scientific reports

OPEN

Dynamic response and vibration suitability analysis of the large-span double-connected structure under coupled wind and pedestrian loads

Shuwang Yang[1], Gang Wang[2], Qiang Xu[1]✉, Junfu He[2], Minghao Yang[1] & Zhiyuan Zhang[1]

Modern buildings increasingly utilize lightweight, high-strength materials and feature high-rise, large-span structural designs. These structures often exhibit low natural frequencies and are susceptible to resonance from low-frequency dynamic loads such as wind and pedestrian loads. This paper focuses on a large-span double-connected structure and analyzes its dynamic response under the combined effects of wind and pedestrian loads. First, a finite element model of the structure was created using ANSYS, and model validity verification and modal analysis were performed. Second, a Fourier-based pedestrian model was used to simulate pedestrian loads and generate time-range data. The pulsating wind speed was generated from the Davenport spectrum using the harmonic superposition method. Wind load time-range data were calculated for different heights using Bernoulli's theorem. Finally, the solution yields information about the dynamic response of the structure. The study revealed maximum vertical comfort ratings in the connecting corridor were achieved when crowd density did not exceed 0.3 persons/m^2. The connecting corridor's most unfavorable horizontal comfort level was evaluated as a medium, except for the 0-degree wind angle condition. This paper provides experience in studying the dynamic response and vibration suitability assessment of the large-span double-connected structure under wind and pedestrian loads.

Keywords Large-span structure, Wind loads, Pedestrian loads, Dynamic response, Vibration suitability

With the continuous advancement of construction technology, lightweight, high-strength building materials, and large-span structural forms are increasingly prevalent in modern architecture. Beyond their beautiful shapes and flexible use of space, these structures possess a characteristic of low natural frequency. However, this characteristic makes them prone to resonance when subjected to low-frequency dynamic loads close to their natural frequencies. This phenomenon can greatly enhance the occupant's perception of structural vibration, causing fear and panic among the occupants. During normal building use, wind loads (usually in the range of 0.1–1.0 Hz[1]) and pedestrian loads (less than 5 Hz[2]) are the most common dynamic loads, and structural comfort problems caused by them occur from time to time. The most significant impacts were the vibration event at the London Millennium Footbridge[3] and the collapse of the Tacoma Strait Bridge[4]. Since then, studying structural vibrations induced by low-frequency dynamic loads has become a popular field.

Piccardo et al.[5] developed an equivalent walking load spectrum model considering the stochasticity of walking parameters from a probabilistic point of view to investigate the vertical vibration of the structure. By conducting human-induced vibration tests, Lee et al.[6] investigated an unusual vertical vibration event at TechnoMart, a 39-story steel building. Chen et al.[7–9] proposed an acceleration response spectrum for predicting the structural response of individuals under walking and jumping activities by statistically analyzing many testers' anthropogenic loading data. Basaglia et al.[10] investigated the human-induced vibration response of large-span wood floor structures by selecting different walking load models. Cao et al.[11] investigated the vibration suitability of large-span lightweight floors for pedestrian loads. Chen et al.[12] conducted field tests on the actual project of a steel truss connecting corridor footbridge and investigated the corresponding structural vibration response and stress state under different pedestrian flow conditions, step frequencies, and motion states.

[1]College of Architecture and Engineering, Liaocheng University, Liaocheng 252000, China. [2]China Railway 17th BureauGroup 1st Engineering Co., Ltd, Qingdao 266000, China. ✉email: xuqiang@lcu.edu.cn

Fig. 1. The Large-span double-connected structure.

Material	Modulus of Elasticity (*pa*)	Poisson's Ratio	Density (kg/m^3)
Q355C steel	2.1×10^{11}	0.3	7850
C50 concrete	3.45×10^{10}	0.2	2550
C30 concrete	3.0×10^{10}	0.2	2550

Table 1. Material physical parameters.

Study[13] points out that the existing problem of structural vibration suitability is mainly attributed to the vertical component coinciding with the step frequencies, which is why most scholars have focused on the human-induced vertical vibration of structures. However, Dey et al.[14] pointed out that pedestrians are more sensitive to horizontal vibration of structures than vertical vibration. For the first time, they evaluated the suitability of pedestrian bridges for horizontal vibration.

Encountering wind loads is inevitable during building use. A growing number of research[15–18] has demonstrated that wind-induced horizontal vibrations in buildings can be perceptible to the human body, potentially leading to issues like motion sickness, sleepiness syndrome, and reduced work performance. This effect is particularly pronounced in the large-span double-connected structure, which typically exhibits lower natural frequencies and inherent structural damping values. This puts such buildings in the frequency range affected by wind loads and makes them more susceptible to resonance with wind loads. Kwok et al.[1] outlined the vibration perception thresholds and occupant comfort evaluation criteria for wind-induced high-rise buildings by analyzing the results of many studies. Wang et al.[19] investigated the wind response and wind loads of super high-rise buildings with different cross-sectional forms and aspect ratios. Li et al.[20] investigated the effect of different wall angle setbacks on the wind load and wind-driven response of rectangular high-rise buildings.

Due to the unique structural form of the large-span double-connected structure, the Spatial large-span corridor connecting the two sides of the main body will assume a function similar to that of a footbridge. However, there are few studies on the dynamic response of structures under coupled wind and pedestrian loads. This paper investigates the dynamic response and vibration suitability of an actual large-span double-connected structure under coupled wind and pedestrian loads. The remaining sections are as follows: Section 2 outlines the large-span double-connected structure and examines its dynamic characteristics. Section 3 details the methodology used to simulate wind and pedestrian loads. Section 4 explores the dynamic response and vibration suitability of the large-span double-connected structure under combined wind and pedestrian loads. Lastly, Section 5 summarizes key findings and conclusions.

Dynamic characterization of the large-span double-connected structure

A large-span double-connected structure in an actual project is shown in Fig. 1. The main buildings on both sides utilize steel frame-support structures, while the connecting corridor between them uses steel truss structures. The building has 18 floors with a total height of 79.4 m. The main building has a plan dimension of 50.4 m × 25.2 m. The plan dimension of the corridor is 58.8 m×25.2 m, and the elevation is 67.125 m ~ 79.4 m. The truss structure reaches a height of 12.275 m (including 3.2 m of decorative steel frames), and the podium is 13.5 m high. The spatial long-span corridor is connected to the main building on the east and west sides through box-type steel columns, beams, and supports. The stringers of the connecting corridor are connected by steel beams and horizontal supports. The steel type is Q355C, the concrete type used for the floor slab is C30, and the concrete type used for the steel pipe concrete columns is C50. Detailed material parameters are provided in Table 1.

To better understand the dynamic characteristics of the large-span double-connected structure, we established a finite element model by ANSYS. In this study, BEAM188 cells are used to simulate the steel beams and meshed along the length of 0.5 m. The reinforced concrete floor slab is modeled using a SHELL181 cell and meshed along the length and width of the concrete floor slab with dimensions of 0.6 m×0.6 m. Steel pipe concrete columns were modeled using BEAM188 cells with custom cross sections, and the steel pipe concrete columns meshed along the length of 0.5 m. The finite element model of the large-span double-connected structure is shown in Fig. 2.

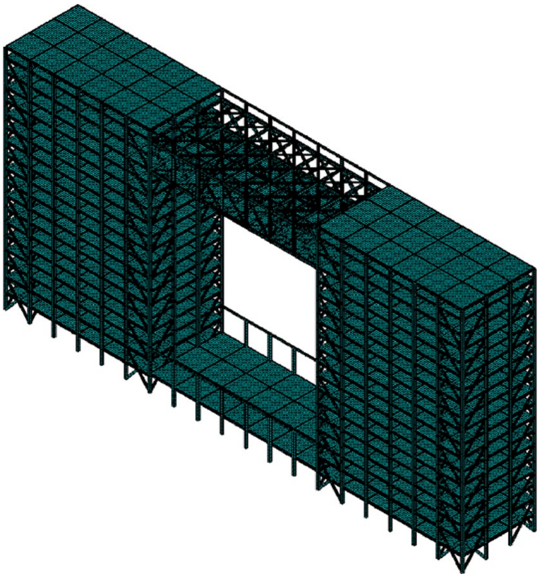

Fig. 2. Finite element model of the large-span double-connected structure.

Location	Horizontal lateral peak acceleration (m/s^2)			Vertical peak acceleration (m/s^2)		
	Control	2-fold grid encryption	Errors (%)	Control	2-fold grid encryption	Errors(%)
The center point of the left main body connection position	0.2623	0.2595	-1.067	0.05413	0.05399	-0.259
The center point of the right main body connection position	0.2692	0.2602	-3.343	0.04245	0.04160	-2.002

Table 2. Finite element mesh accuracy validation.

Order	Frequency(Hz)	Order	Frequency(Hz)
1	0.56322	6	2.1836
2	0.58752	7	2.2019
3	0.63914	8	2.2390
4	1.9272	9	2.9925
5	2.1071	10	3.6387

Table 3. The first 10th-order natural frequencies of the large-span double-connected structure.

The vibration response of the large-span double-connected structure under coupled pedestrian and wind loads is within the scope of normal service condition analysis, and its displacement and acceleration responses mainly occur in the elastic phase. Therefore, we adopt a linear elasticity principal relationship for the elastic analysis of each member, disregarding the reinforcement and slip relationship in the concrete slab and focusing solely on the concrete and steel beams.

Wang et al.[21] pointed out that when the cell length was divided into 0.5 m, the mid-span displacement time range and acceleration time range had errors with the theoretical solution but were very close to the theoretical solution. Based on the above study, we carried out structural meshing of BEAM188 cells according to the size of 0.5 m, and 0.25 m and verified the mesh dependence. The results are shown in Table 2 below.

Table 2 shows that the maximum computational error of finite element is 3.343% when using encrypted and unencrypted meshes, which meets the requirement of less than 5% engineering computational error. Therefore, this paper does not carry out the mesh encryption treatment at the connection between the main body and the connecting corridor.

The modal analysis allows us to determine a structure's natural frequencies and mode shapes and calculate its Rayleigh damping coefficient. Higher-order modes can exhibit coupling effects in complex structures, which may lead to intricate dynamic behavior. Therefore, considering these higher-order modes is crucial for accurately predicting the dynamic response and identifying potential weak points in the structure[22]. From the modal analysis, we have derived the first 10th-order natural frequencies of the large-span double-connected structure as shown in Table 3. Additionally, the first 10th-order mode shapes are shown in Fig. 3.

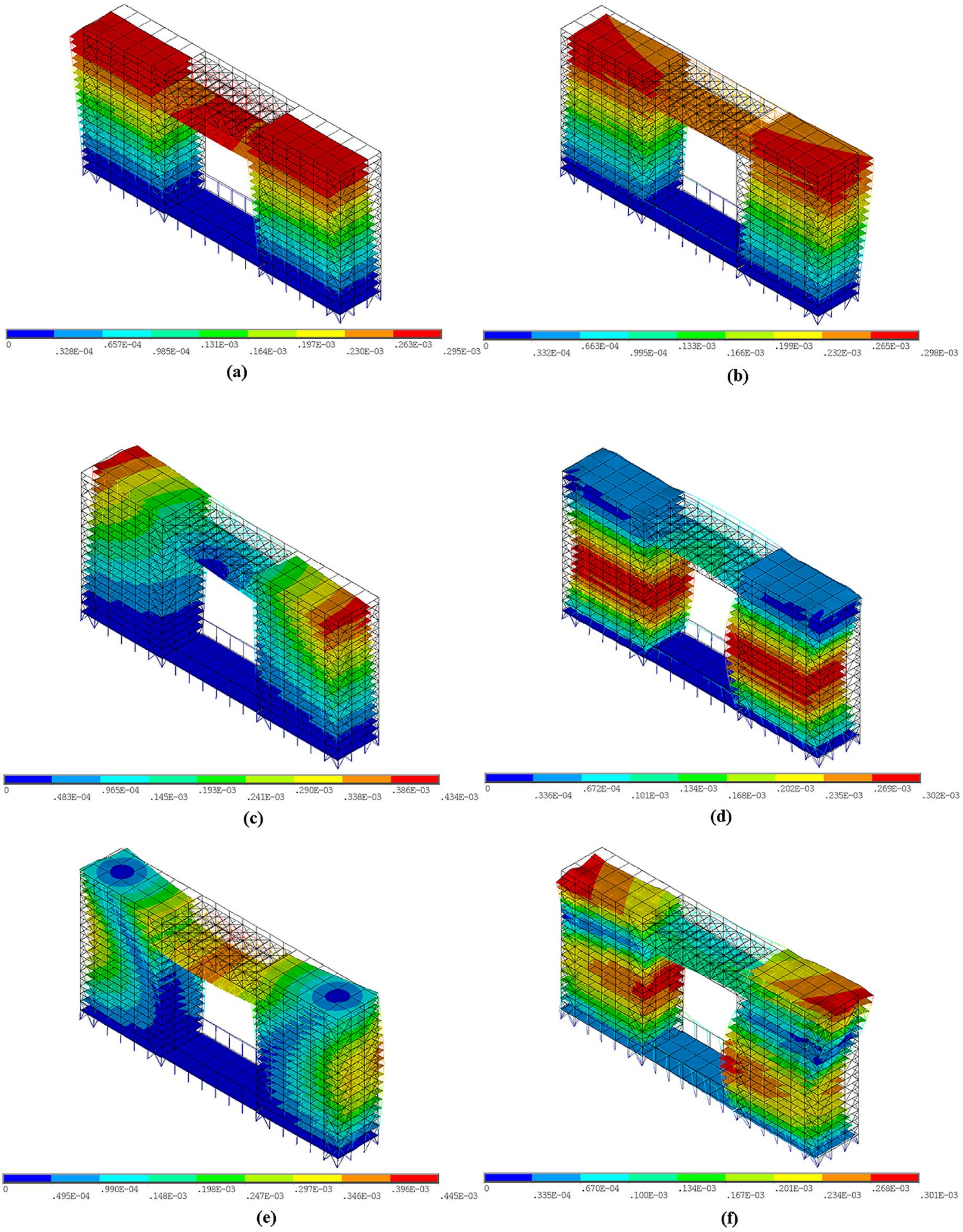

Fig. 3. The first 10th-order mode shapes of the large-span double-connected structure.

From Fig. 3, the 1st order mode is horizontal lateral, the 2nd order mode is a horizontal longitudinal mode, the 3rd and 9th order modes are torsional, the 4th order mode is horizontal longitudinal-vertical bending coupled, the 5th order mode is horizontal lateral-torsional coupled, the 6th and 8th order modes are horizontal longitudinal-torsional coupled, and the 7th and 10th order modes are vertical bending-torsional coupled.

According to Building Structural Load Code[23], the fundamental self-oscillation period of a tall steel building can be estimated using the following equation:

$$T = (0.1 \sim \ 0.15)\, n \tag{1}$$

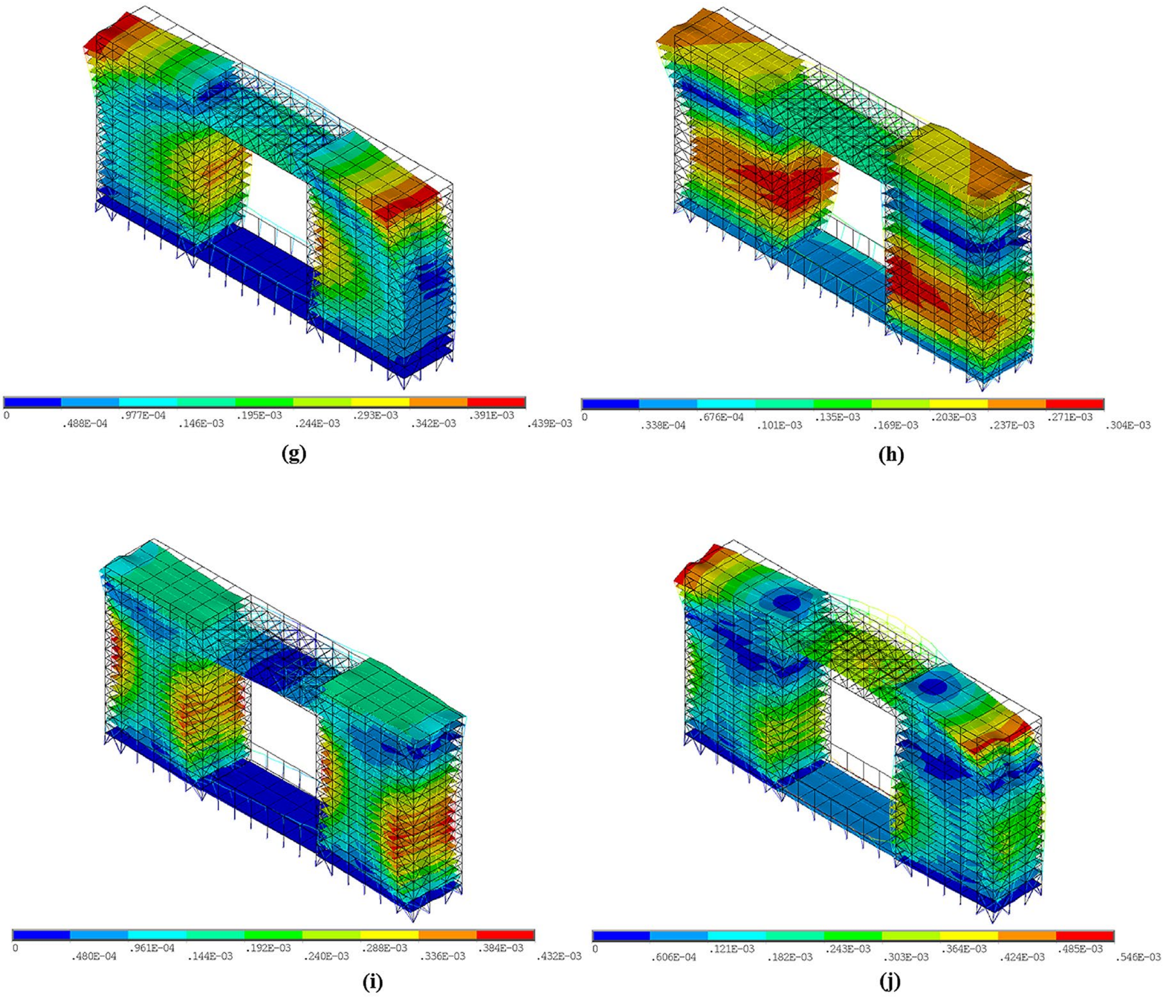

Figure 3. (continued)

Where n is the total number of floors in the building.

The fundamental self-oscillation period of the large-span double-connected structure was calculated using Eq. (1) to range between 1.8 s and 2.7 s. As shown in Table 2, the first-order natural frequency of vibration for this structure is 0.56322 Hz, and the fundamental self-oscillation is 1.78 s. This closely aligns with the theoretical estimate from empirical formulas, validating the validity of our established finite element model.

Kwok et al.[1] pointed out that wind-induced vibration frequencies of high-rise buildings are usually in the range of 0.1–1.0 Hz. Živanović et al.[24] pointed out that the normal walking step frequency of pedestrians obeys a Gaussian distribution with a mean value of 1.87 Hz and a standard deviation of 0.186 Hz. Schlaich et al.[2] pointed out that human-induced vibration frequencies are usually in the low-frequency range of less than 5 Hz. From Table 3, it can be seen that the first 3rd-order natural frequencies of the structure are within the sensitive range of wind-induced vibration, while the first 10th-order natural frequencies are within the sensitive range of human-induced vibration. Thus, investigating the dynamic response of the large-span double-connected structure, particularly the spatial large-span corridor, under combined wind and pedestrian loads is crucial.

Dynamic excitation and equations of motion of the large-span double-connected structure

According to the theory of structural dynamics, the equations of motion of the large-span double-connected structure under dynamic excitation can be described by the following equation [25]:

$$M\ddot{X}+C\dot{X}+KX=\sum_{i=1}^{N}F_i\left(t\right) \tag{2}$$

Where M, C, and K are the mass, damping, and stiffness matrices of the large-span double-connected structure, respectively. $F_i(t)$ is the external dynamic excitation, which is mainly considered in this paper as pedestrian loads and wind loads.

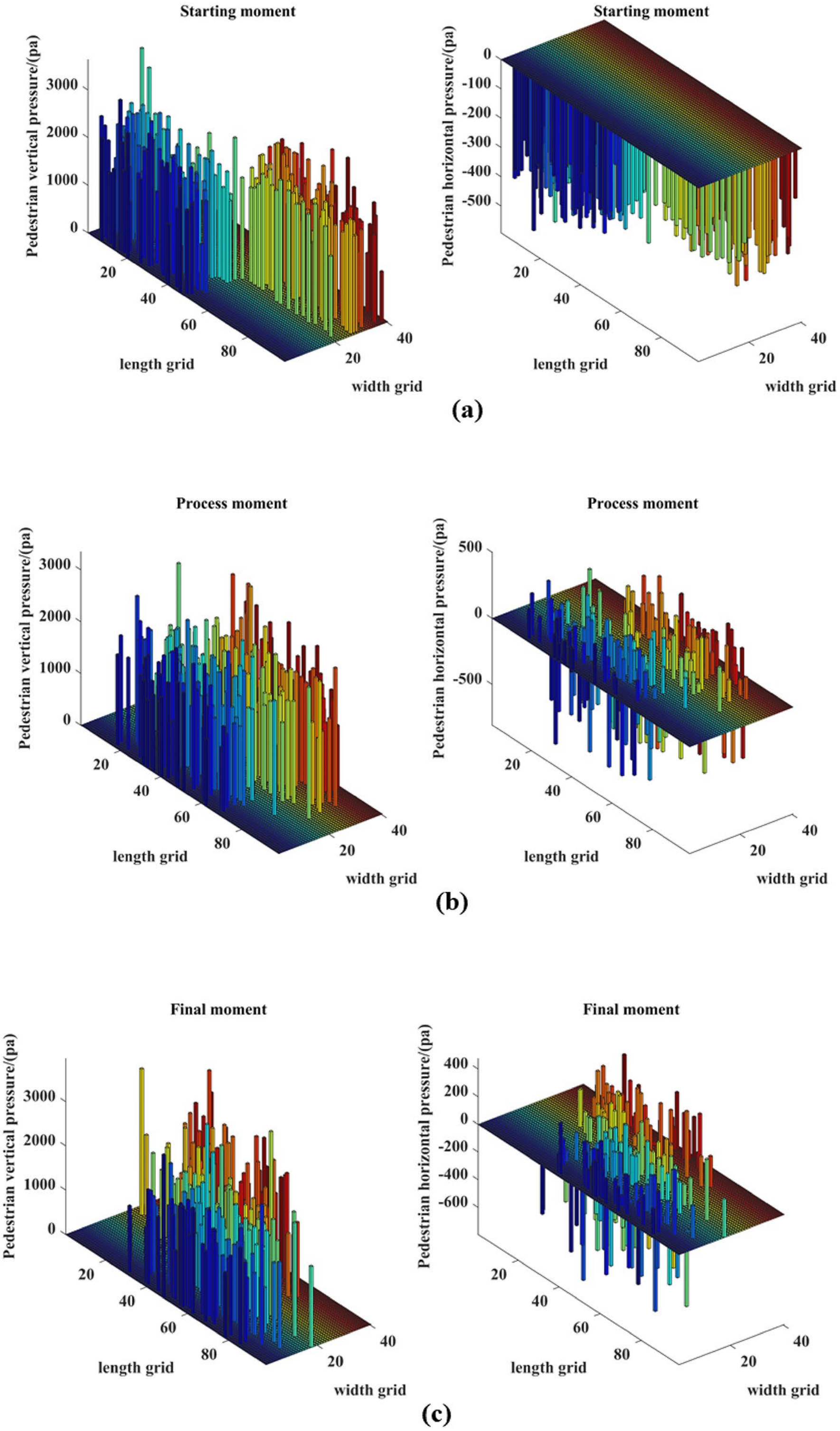

Fig. 4. Pedestrian positions and corresponding vertical and horizontal lateral pedestrian pressures at different moments for a pedestrian density of 0.2 person/m^2. (**a**) Pedestrian position distribution and pressure magnitude at the starting moment. (**b**) Pedestrian position distribution and pressure at the process moment. (**c**) Pedestrian position distribution and pressure at the final moment.

Pedestrian loads

Pedestrian load is a three-dimensional force[26–28] that consists of a vertical component, a horizontal lateral component, and a horizontal longitudinal component. However, the horizontal longitudinal force is generally considered negligible. The horizontal lateral component arises from the horizontal movement of the center of gravity during walking, occurring at half the step frequency[13]. In time-domain analysis, pedestrian loading models are often treated as deterministic periodic processes, represented by Fourier series[29]. The study[27] shows that the load models for the vertical and horizontal lateral components of pedestrian loads are significant for the vibration suitability analysis of large-span structures. The pedestrian load model selected in this paper is as follows:

$$\left\{\begin{array}{c} F_z\left(t\right) = G\left[1 + \sum_{i=1}^{n} \alpha_{zi} sin\left(2i\pi\ f_p t - \phi_{zi}\right)\right] \\ F_x\left(t\right) = G\sum_{i=1}^{n} \alpha_{xi} sin\left(i\pi\ f_p t - \phi_{xi}\right) \end{array}\right. \tag{3}$$

Where $F_z(t)$ and $F_x(t)$ are the vertical and horizontal lateral walking excitations, respectively. G is the person's resting gravity, f_p is the person's step frequency, and n is the number of orders considered in the model. α_{zi} and α_{xi} are the i-th-order dynamic loading factors in the vertical and horizontal lateral directions, respectively. φ_{zi} and φ_{xi} are the i-th-order harmonic phase angles in the vertical and horizontal lateral directions, respectively. The specific parameters in the above Eq. (3) are described in Literature[27].

Based on the above Fourier series expression of the pedestrian load model, we established a pedestrian load model considering the randomness of pedestrian parameters, walking routes, and the number of pedestrians. The pedestrian load is applied to the large-span double-connected structure by this model, and the detailed description of this pedestrian load modeling method is shown in Literature[30]. Taking the pedestrian density of 0.2 person/m^2 as an example, Fig. 4 illustrates the distribution of the pedestrian positions and the magnitude of the resulting vertical and horizontal lateral walking excitation values at different moments.

Wind loads

Calculation of wind speed

In general, the wind speed v comprises the average wind speed and the pulsating wind speed[31]. This relationship can be expressed by the following equation:

$$v = v_s + v_d \tag{4}$$

Where v_s denotes the average wind speed at any height of the structure. v_d denotes the pulsating wind speed at any height of the structure.

According to Building Structural Load Code[23], the average wind speed v_s at any height of the structure can be described by the following exponential law:

$$v_s\left(z\right) = v_{10}\left(\frac{z}{10}\right)^{\alpha} \tag{5}$$

Where v_{10} denotes the basic wind speed at a height of 10 m above ground level, z denotes the height of the structure above ground level, and α denotes the ground roughness index, typically taken as 0.22.

According to Code[23], the basic wind pressure in the area where the large-span double-connected structure is located is 0.5 KN/m^2. Based on the basic relationship between wind speed and wind pressure, the average wind speed v_{10} at a standard height of 10 m above the ground can be calculated to be 28.4 m/s.

Pulsating wind speeds can be modeled as a zero-mean smooth Gaussian random field, as indicated by most measured data[25]. Under these assumptions, the longitudinal pulsation velocity at any point can be characterized using either the Davenport or the Simiu spectrum. While the Simiu spectrum incorporates wind speed variations at different heights, it is generally applicable to the low-frequency range with frequencies below 0.2 Hz. Conversely, based on empirical observations, Kaimal et al.[32] introduced a spectrum tailored for high frequencies exceeding 0.2 Hz. In addition, the Kaimail and Simiu spectra do not yield a value for the power spectral density $S(\omega) = 0$, whereas the Davenport spectrum yields a value for the power spectral density $S(\omega) = 0$. Taking all these considerations into account, we chose the Davenport spectrum for the calculation of pulsating wind speed[33,34]. The following equation can describe the Davenport spectrum:

$$\left\{\begin{array}{c} S_{v_d}\left(\omega\ \right) = 4kv_{10}^2\frac{f^2}{\omega\left(1+f^2\right)^{4/3}} \\ f = \frac{1200\omega}{v_{10}} \end{array}\right. \tag{6}$$

where $S_{v_d}\left(\omega\ \right)$ is the pulsating wind speed power spectrum. ω is the pulsating wind frequency. k is the ground roughness coefficient, which can be taken as 0.00464 according to the study[35].

Pulsating wind speeds are correlated between two points within a certain distance at the same or different heights. The correlation can generally be described by the mutual power spectral density[36], which can be expressed as:

$$\left\{\begin{array}{c} S_{v_{d1}v_{d2}}\left(\omega\ \right) = \sqrt{S\left(z_1, \omega\ \right)S\left(z_2, \omega\ \right)}e^{-\widehat{f}} \\ \widehat{f} = \frac{\omega\sqrt{C_Z^2\left(z_1 - z_2\right)^2 + C_Y^2\left(x_1 - x_2\right)^2}}{\pi\left[v_s(z_1) + v_s(z_2)\right]} \end{array}\right. \tag{7}$$

Parametric	Value	Parametric	Value
Basic wind pressure	0.5KN/m^2	Simulation time step	0.1s
Geomorphologic category	C	Total Sampling Points	3000
Ground roughness index α	0.22	Initial sampling frequency	0.001 Hz
Target power spectrum	Davenport spectrum	Cutoff frequency	10 Hz
Total simulation time	600s	Frequency increment	0.001 Hz

Table 4. Basic parameters of pulsating wind speed simulation.

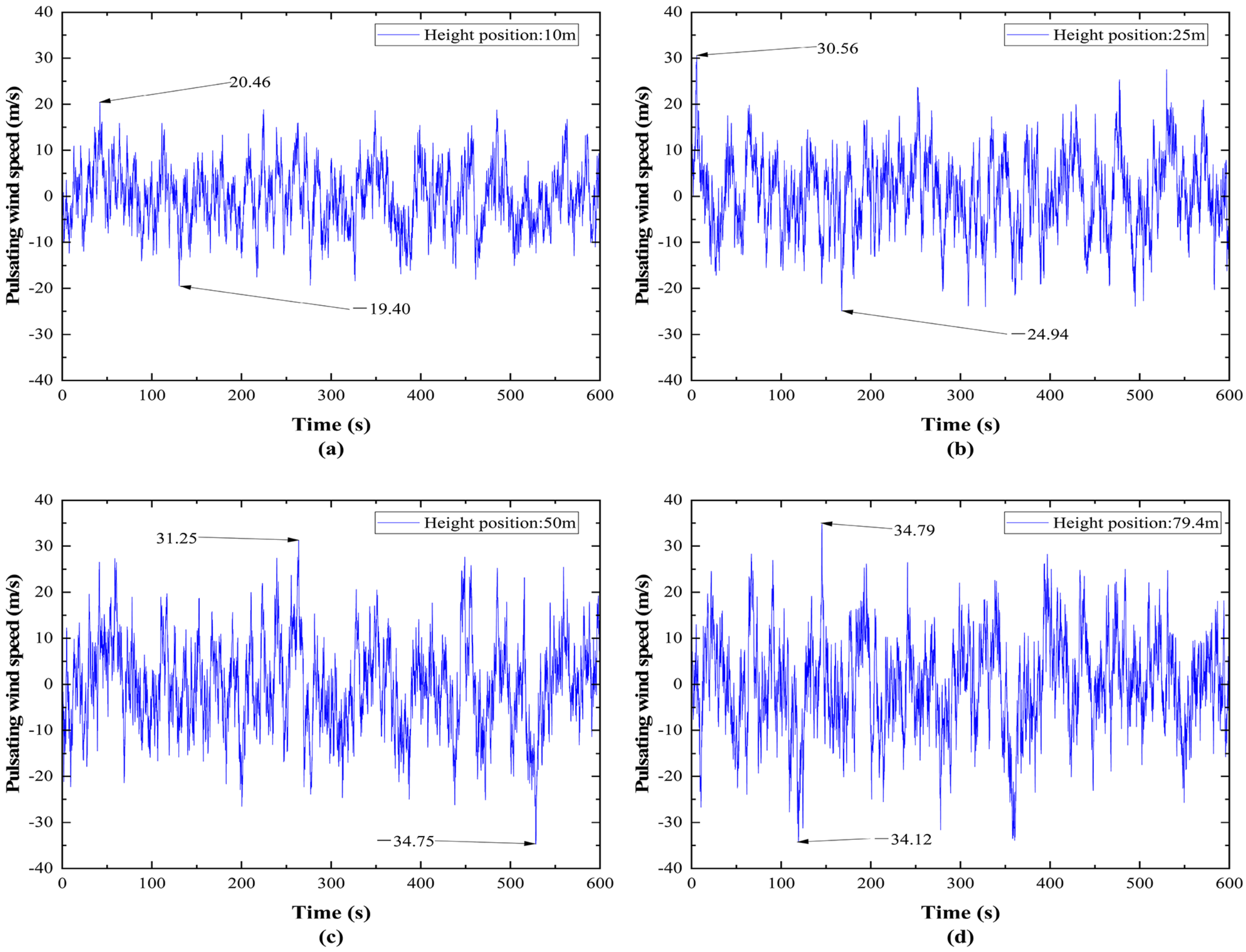

Fig. 5. Time-course curves of pulsating wind speed at different heights. (**a**) Height position: 10 m. (**b**) Height position: 25 m. (**c**) Height position: 50 m. (**d**) Height position: 79.4 m.

Where v_{d1} and v_{d2} denote the pulsating wind speeds at points M_1 and M_2. x_1 and x_2 are the coordinates of point M_1, and z_1 and z_2 are the coordinates of point M_2. C_Z and C_Y are empirically determined attenuation coefficients, generally taken as $C_Z=10$ and $C_Y=16$.

The density function matrix of the pulsating wind speed spectrum with n different or same height points can be expressed by the following equation:

$$S(\omega)=\begin{bmatrix} S_{v_{d1}v_{d1}}(\omega) & \cdots & S_{v_{d1}v_{dj}}(\omega) & \cdots & S_{v_{d1}v_{dn}}(\omega) \\ \vdots & \ddots & \vdots & & \vdots \\ S_{v_{di}v_{d1}}(\omega) & \cdots & S_{v_{di}v_{dj}}(\omega) & \cdots & S_{v_{di}v_{dn}}(\omega) \\ \vdots & & \vdots & \ddots & \vdots \\ S_{v_{dn}v_{d1}}(\omega) & \cdots & S_{v_{dn}v_{dj}}(\omega) & \cdots & S_{v_{dn}v_{dn}}(\omega) \end{bmatrix} \tag{8}$$

Where $S_{v_{di}v_{dj}}(\omega)$ is the mutual power density function at any two points M_i and M_j.

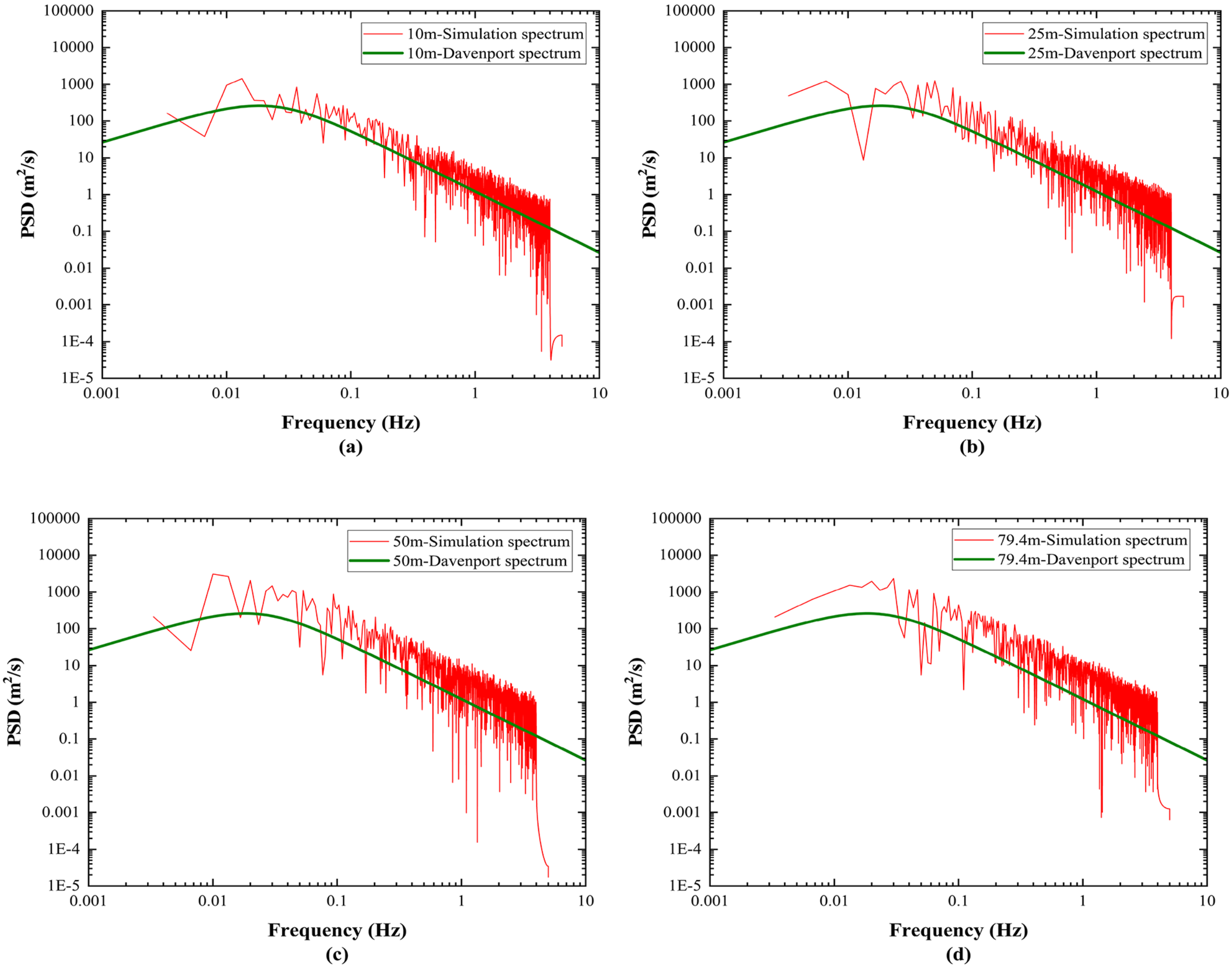

Fig. 6. Comparison of simulated spectra of pulsating wind speed at different heights with Davenport spectra. (**a**) Height position: 10 m. (**b**) Height position: 25 m. (**c**) Height position: 50 m. (**d**) Height position: 79.4 m.

The Cholesky decomposition of the pulsating wind speed spectral density function matrix $S(\omega)$ is performed as follows:

$$\left\{\begin{array}{c} S(\omega) = H(\omega)\cdot H^{*}(\omega)^{T} \\ H(\omega) = \begin{bmatrix} H_{v_{11}}(\omega) & \cdots & 0 & \cdots & 0 \\ \vdots & \ddots & \vdots & & \vdots \\ H_{v_{i1}}(\omega) & \cdots & H_{v_{ii}}(\omega) & \cdots & 0 \\ \vdots & & \vdots & \ddots & \vdots \\ H_{v_{n1}}(\omega) & \cdots & H_{v_{ni}}(\omega) & \cdots & H_{v_{nn}}(\omega) \end{bmatrix} \end{array}\right. \tag{9}$$

where $H^{*}(\omega)^{T}$ is the conjugate transpose of $H(\omega)$.

For the multidimensional vector pulsating wind speed spectral density function matrix $S(\omega)$, the pulsating wind speed v_d can be described by the following equation:

$$\left\{\begin{array}{c} v_{di}(t) = \sum_{i=1}^{m}\sum_{j=1}^{N} \left|H_{mi}(\omega_j)\right| \sqrt{2\Delta\omega}\cos\left[\omega_j t + \psi_{mi}(\omega_j) + \theta_{ij}\right], m = 1,2,\ldots,n \\ n_j = n_d + (j-1/2)\Delta n, j = 1,2,\ldots,N \end{array}\right. \tag{10}$$

Where N denotes the division of the pulsating wind speed power spectrum into N identical parts in the frequency range. $\Delta\omega = \omega/N$ is the frequency increment. $\omega_j = j\cdot\Delta\omega$ is a recursive increment in the frequency domain. $|H_{mi}(\omega_j)|$ is the mode of $H(\omega)$. ψ_{mi} is the phase angle between two different points. θ_{ij} is a random number uniformly distributed in the range $[0,2\pi]$.

The foundational parameters for simulating pulsating wind speeds in the area near the large-span double-connected structure are shown in Table 4.

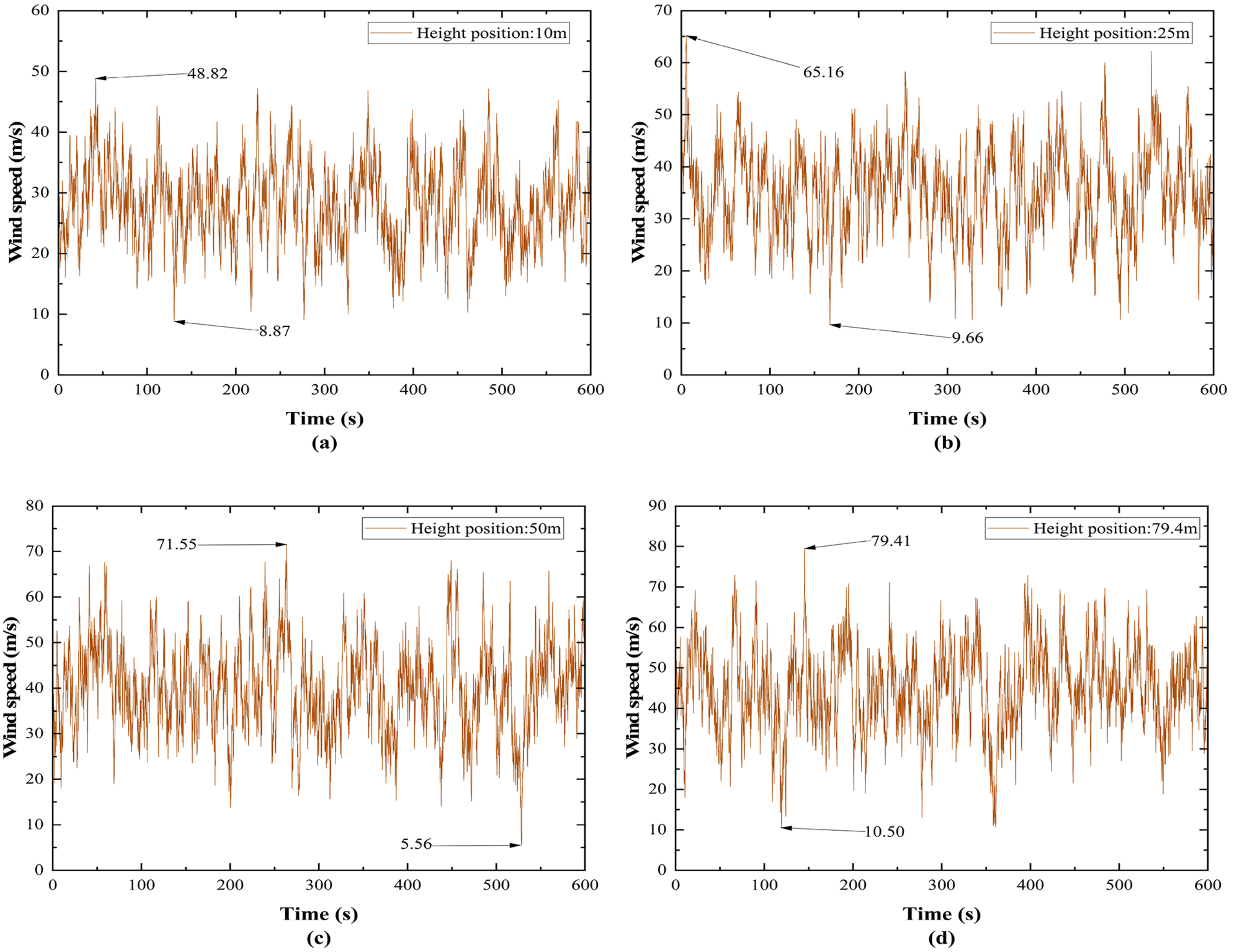

(a) (b) (c) (d)

Fig. 7. 10-min wind speed time-course curve at different heights. (**a**) Height position: 10 m. (**b**) Height position: 25 m. (**c**) Height position: 50 m. (**d**) Height position: 79.4 m.

Geomorphologic category	Height from the ground	Coefficient of variation of wind pressure height μ_{zi}
C	5	0.65
	10	0.65
	15	0.65
	20	0.74
	30	0.88
	40	1.00
	50	1.10
	60	1.20
	70	1.28
	80	1.36

Table 5. Values of wind pressure height variation coefficients for the large-span double-connected structure.

The pulsating wind speed is simulated by the harmonic superposition method, and the 10-min time-course curves of pulsating wind speed at different heights are obtained as shown in Fig. 5. The pulsating wind speed time profile obtained from the simulation is converted into a pulsating wind speed spectrum and compared with the Davenport spectrum. The results are shown in Fig. 6.

From Fig. 6, the simulated spectral curves of pulsating wind speed at different heights basically coincide with the fluctuation trend of Davenport spectral curves. This shows that the simulated time-course curve of pulsating wind speed can better meet the requirement of randomness and correlation of actual pulsating wind speed in time and space. The deviation of the two spectral curves is because the Davenport spectra are derived

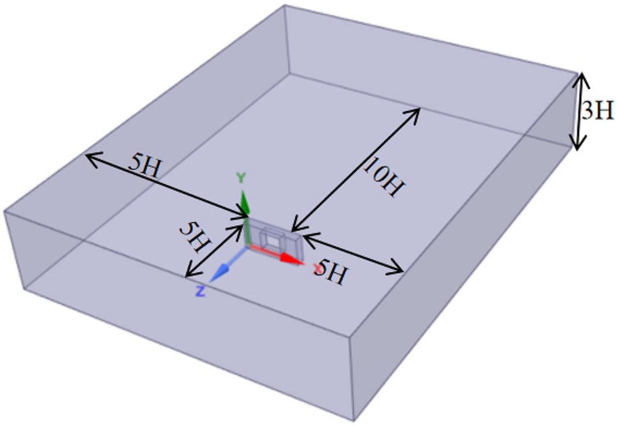

Fig. 8. Schematic distribution of the wind field domain and the location of the large-span double-connected structure.

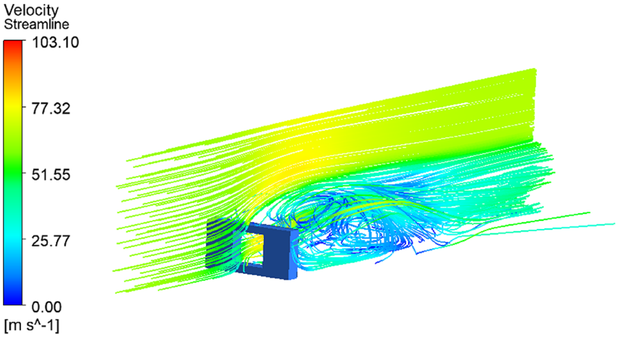

Fig. 9. Schematic diagram of wind velocity streamlines at the center section of the large-span double-connected structure at a 0-degree wind angle.

by averaging the measured wind speeds at different heights, which does not reflect the relationship between spectra and height. Thus, the Davenport spectrum somewhat overestimates the energy of wind speeds in the high-frequency region and underestimates the energy in the low-frequency region[25].

The 10-min wind speed time-course curve at different node heights calculated from Eq. (4) is shown in Fig. 7.

Calculation of wind loads

According to Study[37], the standard values of wind loads acting vertically on the structure are calculated as follows:

$$F_{zi} = \mu_{si} \mu_{zi} w_i A_i \tag{11}$$

Where F_{zi} represents the wind loads at node area *i* at height Z. μ_{si} denotes the coefficient for the wind load body shape. μ_{zi} represents the coefficient for the change in wind pressure with height. w_i represents the wind pressure at height Z, and A_i denotes the windward area exerting vertical pressure on the building surface.

According to Code[23]μ_{zi} taken as in Table 5.

Currently, there is no standardized wind load body shape coefficient specified in codes and standards for large-span double-connected structural forms. For complex shapes, wind load body shape coefficients do not yield theoretical results and are typically derived through wind tunnel tests or numerical simulations. To accurately apply wind loads to finite element models, this study employs Computational Fluid Dynamics methods[19,38] to calculate shape coefficients.

Wind pressure distribution characteristics of the large-span double-connected structure To conduct simulated wind tunnel tests, it is essential to establish a suitable wind field domain. According to Code[39], the blockage ratio between the structure and the wind field domain should not exceed 5%. The blockage ratio can be calculated by the following equation:

$$\eta = \frac{A_m}{A_c} \tag{12}$$

Where A_c is the cross-sectional area of the wind field domain. A_m is the maximum windward area of the building.

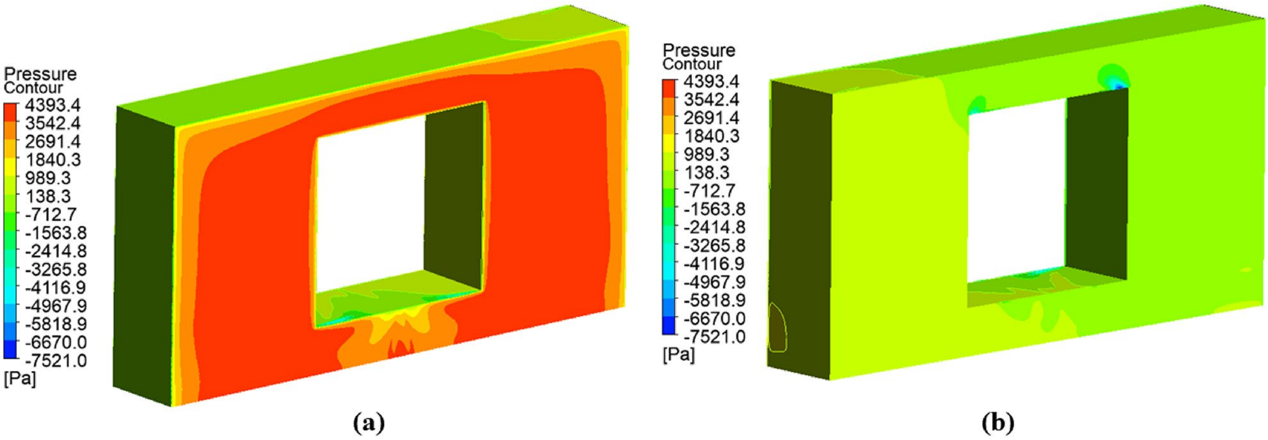

Fig. 10. Cloud diagram of wind pressure distribution for the large-span double-connected structure at 0-degree wind angle. (**a**) Wind pressure distribution on the windward side. (**b**) Wind pressure distribution on the leeward side.

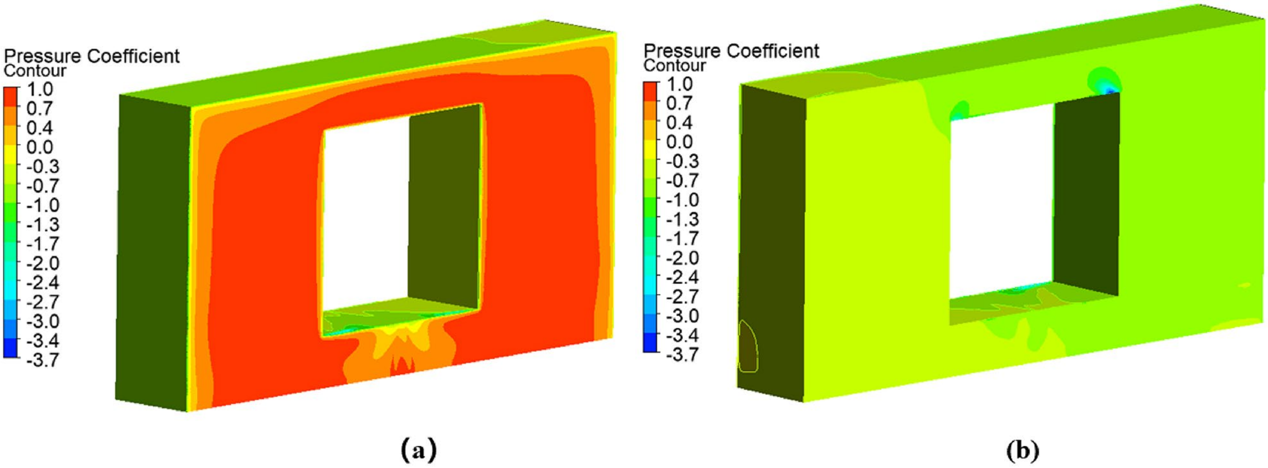

Fig. 11. Cloud diagram of wind pressure coefficient distribution for the large-span double-connected structure at 0-degree wind angle. (**a**) Wind pressure coefficient distribution on the windward side. (**b**) Wind pressure coefficient distribution on the leeward side.

To more accurately simulate the wind pressure distribution characteristics of the structure in the wind field, we have parameterized the wind field domain with the maximum height (H) of the building. Define the wind angle as the angle formed by the large-span double-connected structure and the plane where the XY axis is located, and the wind angle is positive when it rotates around the Y axis in a counterclockwise direction. Define the minimum grid size of the wind field domain as 0.5 m and the maximum size as 15 m with a growth rate of 1.2. At the same time, local mesh encryption was carried out for the large-span double-connected structure with a mesh size of 0.5 m. The large-span double-connected structure and wind field domain model at a 0-degree wind angle are shown in Fig. 8.

Combining Eq. (12) with the structural dimensional parameters, we calculate the maximum blockage ratio η of the system to be 4.2%. Fig. 9 illustrates that positioning the large-span double-connected structure at one-third of the distance from the wind field domain entrance ensures uninterrupted flow throughout the domain, preventing backflow at the exit boundary. This confirms the rationale and effectiveness of our defined wind field domain.

Natural winds in the atmospheric boundary are turbulent winds with randomness and complexity in spatial and temporal properties. Commonly used turbulence models[40,41] include the k-ε model, the k-ω model, the Reynolds Stress (RMS) model, and the Large Eddy Simulation (LES) model. In this paper, the SST k-ω model[38] of the k-ω model is chosen, which combines the advantages of the k-ω model for calculations in the near-wall region and the k-ε model for calculations in the far field. The turbulence intensity I_z can be calculated from the following equation [39]:

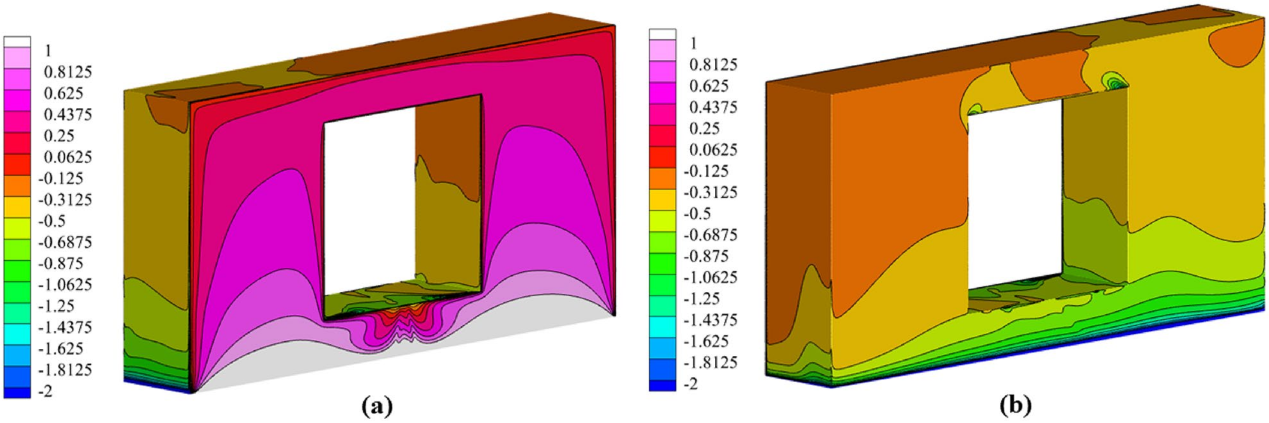

Fig. 12. Cloud diagram of the wind load body shape coefficient distribution for the large-span double-connected structure at a 0-degree wind angle. (**a**) Windward wind load body shape factor distribution. (**b**) Leeward wind load body shape factor distribution.

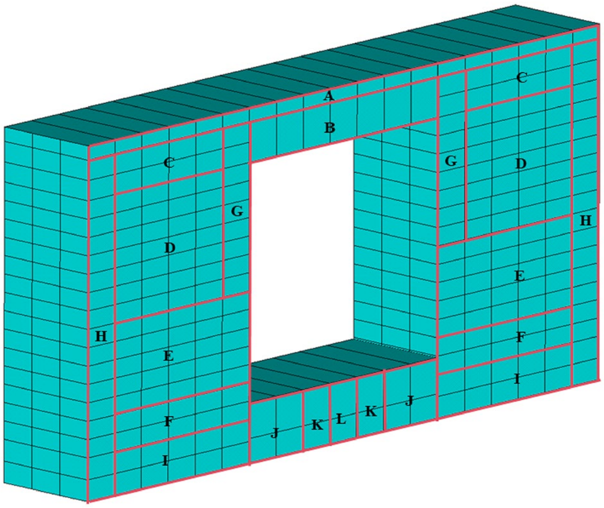

Fig. 13. Schematic of dividing the surface area on the windward side of the large-span double-connected structure at a 0-degree wind angle.

$$I_z = I_{10}\left(\frac{z}{10}\right)^{-\alpha}, z_b \leq z \leq z_g \tag{13}$$

Where I_z is the degree of turbulence obtained at height Z. I_{10} is the nominal degree of turbulence at a standard height of 10 m, which takes the value of 0.23. α is the mean wind profile index, which takes the value of 0.22. Z_b is the height of profile initiation, which takes the value of 15 m. Z_g is the height of gradient winds, which takes the value of 450 m.

The turbulent kinetic energy *k* and the dissipation rate *ω* can be calculated from the following equation [38,42]:

$$\begin{cases} k = 1.5(v_z \times \mathrm{I_z})^2 \\ \omega = \frac{k^{0.5}}{(C_\mu^{0.25} \times L_\mu)} \end{cases} \tag{14}$$

Where C_μ is the turbulence constant, typically taken as 0.09. v_z represents the velocity at height Z. L_μ denotes the turbulence integration scale, which can be expressed by the following equation [37]:

$$L_\mu = \begin{cases} 100, z \leq 30m \\ 100(z/30)^{0.5}, 30m \leq z \leq z_g \end{cases} \tag{15}$$

The inlet boundary condition of the wind field domain is defined by Eq. (5). The outlet boundary condition adopts the fully developed free outflow boundary condition, i.e., any physical quantity of the flow field has zero

Building surface area	Height range (m)	Breadth(m)	μ_{si}
A	76.2—79.4	159.6	0.156
B	67.125—76.2	58.8	0.438
C	67.125—76.2	33.6	0.250
D	38.425—67.125	33.6	0.438
E	17.925—38.425	42	0.675
F	9.725—17.925	42	0.813
G	38.425—76.2	8.4	0.438
H	0—76.2	8.4	0.156
I	0—9.725	42	1
J	0—13.5	16.8	0.906
K	0—13.5	8.4	0.625
L	0—13.5	8.4	0.513

Table 6. Building Windward surface zoning information.

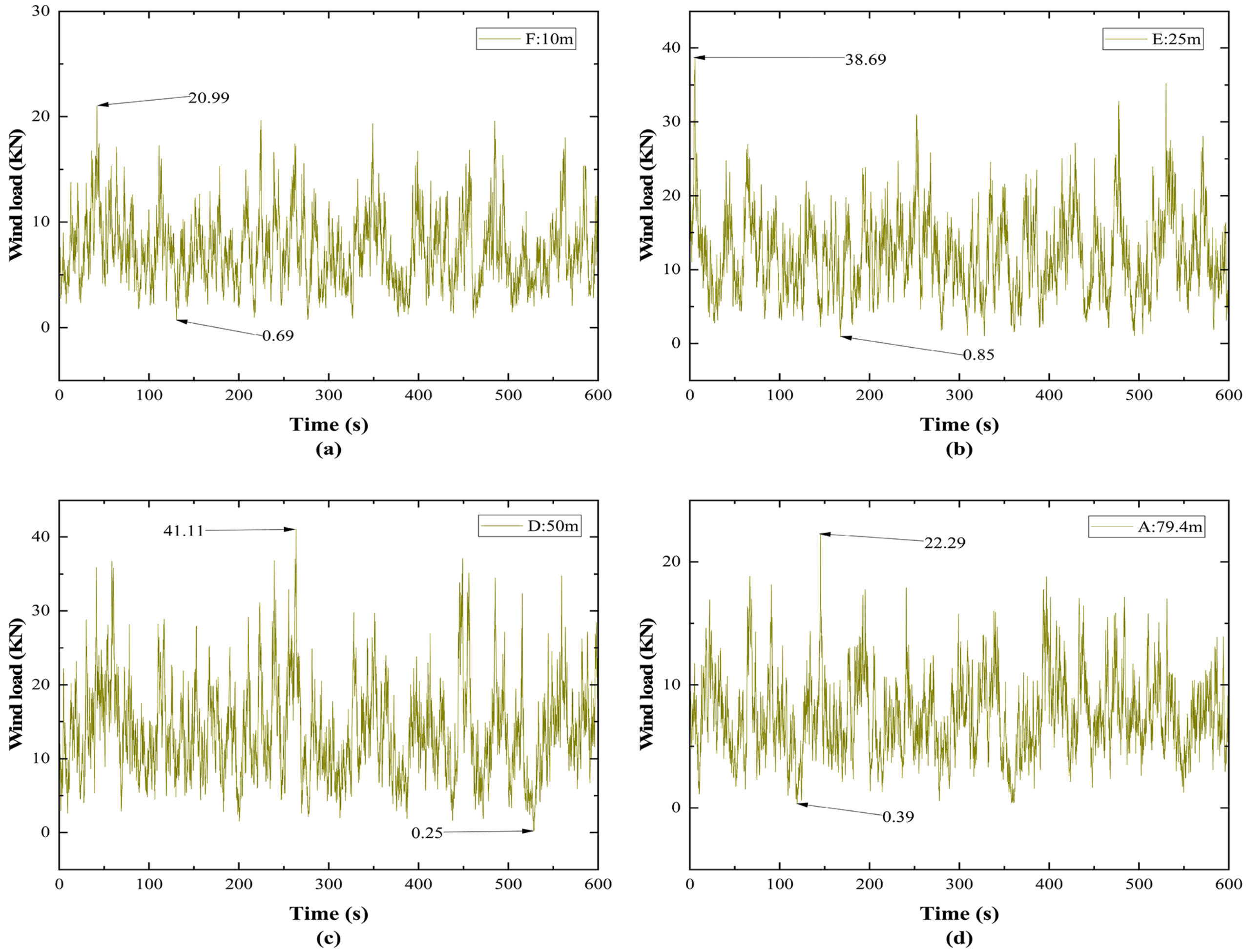

Fig. 14. Time-course curve of wind load at different heights on the windward face of the large-span double-connected structure at 0-degree wind angle. (**a**) Height position: 10 m. (**b**) Height position: 25 m. (**c**) Height position: 50 m. (**d**) Height position: 79.4 m.

Response point	Height (m)	Location	Response point	Height (m)	Location
1	26.125	Left main body span center	6	67.125	Corridor spanning center
2	26.125	Right main body span center	7	67.125	Right main body span center
3	50.725	Left main body span center	8	67.125	The center point of the left main body connection position
4	50.725	Right main body span center	9	67.125	The center point of the right main body connection position
5	67.125	Left main body span center			

Table 7. Response point location information.

Loading condition	Angle of wind	Crowd density (person/m^2)	Pedestrian to structural mass ratio (%)
1	0°	0.1	0.62
2		0.2	1.24
3		0.3	1.86
4		0.4	2.48
5		0.5	3.10
6	45°	0.1	0.62
7		0.2	1.24
8		0.3	1.86
9		0.4	2.48
10		0.5	3.10
11	90°	0.1	0.62
12		0.2	1.24
13		0.3	1.86
14		0.4	2.48
15		0.5	3.10

Table 8. Coupled wind and pedestrian loading conditions.

gradient along the outlet's normal direction. The surface of the large-span double-connected structure and the ground are smooth walls with no slip. The boundary conditions for the wind field utilize free-slip walls on both sides and the top. Iterative convergence is determined with a residual threshold of 10^{-4}, employing the SIMPLE algorithm for a solution. Momentum, Turbulent Kinetic Energy, and Specific Dissipation Rate are treated in Second Order Upwind format. As an illustration at a 0-degree wind angle, the wind pressure distribution cloud map for the large-span double-connected structure is computed and depicted in Fig. 10.

The dimensionless wind pressure coefficient C_{pi} is usually used in structural wind engineering to characterize the wind pressure distribution, which can ignore the effects of other parameters and make the results highly generalizable. The wind pressure coefficient can be calculated by the following equation [20,41]:

$$C_{pi} = \frac{p_i - p_0}{0.5\rho\, v_{10}^2} \tag{16}$$

Where P_i represents the pressure value at measurement point *i*. P_0 denotes the static pressure value at a reference point located at a standard height of 10 m. ρ stands for air density.

The cloud diagram of wind pressure coefficient distribution for the large-span double-connected structure calculated from the above Eq. (16) is shown in Fig. 11.

<u>Calculation of the wind load body shape factor for the large-span double-connected structure</u> The wind load body shape coefficient can be calculated using the following equation:

$$\mu_{si} = C_{pi}\left(\frac{10}{Z_i}\right)^{2\alpha} \tag{17}$$

Where Z_i represents the height at measurement point *i*, and α denotes the ground roughness index.

Figure 12 displays the cloud diagram illustrating the wind load body shape coefficient distribution for the large-span double-connected structure at a 0-degree wind angle, calculated using Eq. (17).

Coupled with the wind load body shape coefficient distribution cloud diagram for the large-span double-connected structure, Fig. 13 illustrates the surface zoning on the windward side of the large-span double-connected structure at a 0-degree wind angle. Specific zoning details for localized building surfaces are provided in Table 6.

From Eq. (11), the time-course curve of wind load at different heights on the windward face of the large-span double-connected structure at a 0-degree wind angle is calculated, as shown in Fig. 14.

Crowd density (person/m²)	Peak acceleration under pedestrian loading(m/s²)		Peak acceleration under coupled pedestrian and wind loads(m/s²)					
			0-degree wind angle		45-degree wind angle		90-degree wind angle	
	Vertical	Horizontal lateral	Vertical	Horizontal lateral	Vertical	Horizontal lateral	Vertical	Horizontal lateral
0.1	0.1619	0.0040	0.1474	0.3104	0.1351	0.1821	0.1546	0.0215
0.2	0.3844	0.0080	0.3588	0.3051	0.3388	0.1821	0.3580	0.0246
0.3	0.4830	0.0108	0.4546	0.3011	0.4281	0.1825	0.4412	0.0260
0.4	0.6082	0.0146	0.5930	0.2942	0.5700	0.1831	0.5500	0.0282
0.5	0.7435	0.0176	0.7063	0.2915	0.6942	0.1835	0.6679	0.0312

Table 9. Dynamic response information of response point 6 under pedestrian loading and coupled pedestrian and wind loading.

Dynamic response analysis and vibration suitability evaluation of the large-span double-connected structure under coupled wind and pedestrian loads

A SURF154 cell was applied to the surface of the finite element model of the large-span double-connected structure to convert wind speed into wind pressure for structural loading. At the same time, pedestrian loads were applied to the connecting corridor section of the structure. The transient dynamic analysis of the large-span double-connected structure was conducted using the full method. To accurately capture the dynamic response of the structure, the loading sub-step was set to 50 to ensure precise measurement of acceleration variations. Rayleigh damping was introduced in the FE model to account for structural damping effects. According to the structural dynamics, the Rayleigh damping coefficient can be calculated by the following equation:

$$\begin{cases} \alpha = \frac{2\omega_i\omega_j\xi}{\omega_i+\omega_j} \\ \beta = \frac{2\xi}{\omega_i+\omega_j} \end{cases} \tag{18}$$

where ω_i is the i th order natural frequency of the structure and ω_j is the j th order natural frequency of the structure. ξ is the damping ratio of the structure and takes the value of 2%.

Dynamic response analysis of the large-span double-connected structure

To compare the dynamic response of the large-span double-connected structure at different locations, we set up nine response points for the study. The specific location information of the response points is shown in Table 7.

To reduce the impact of wind load randomness on the finite element solution. Ten sets of wind load data were randomly generated for this study, and the average of these sets was employed as the final wind load applied to the structure. This study considered three wind loading conditions at different wind angles due to the symmetry of the large-span double-connected structure. Additionally, five pedestrian loading conditions were established, varying in crowd densities. The maximum mass ratio of pedestrians to the spatial long-span corridor is 3.1% across the five pedestrian loading conditions. Since the mass of the pedestrians is much smaller than the total mass of the structure, their effect on the mass of the whole system can be ignored. Details of the specific loading condition combinations are provided in Table 8.

We compared and analyzed the peak acceleration of response point 6 under pedestrian loading and coupled pedestrian and wind loading, and the results are shown in Table 9.

According to the data in Table 9, considering the structure under the coupling of pedestrian and wind loads, the wind load has a certain inhibiting effect on the vertical acceleration of the structure caused by pedestrian loads. With the increase in crowd density, the peak vertical acceleration of the structure considering wind loads is reduced by 2.56–9.84% compared to that when only pedestrian loads are considered. This phenomenon indicates that the presence of wind loads improves the vertical comfort of the structure to some extent. Meanwhile, the contribution of wind loads to the horizontal lateral peak acceleration of the structure under the coupled pedestrian and wind loads ranges from 93.96 to 98.71%. This indicates that the effect of pedestrian loads on the horizontal transverse dynamic response of the structure is small. Therefore, it is necessary to consider the coupling of wind and pedestrian loads when performing structural vibration suitability assessment.

We conducted finite element analyses under various coupled load conditions to determine the acceleration response of the large-span double-connected structure under different scenarios. Taking response point 6 located at the center of the connecting corridor as an example, Fig. 15 illustrates the acceleration response curves under different pedestrian loading conditions at a 0-degree wind angle. Figure 16 shows the acceleration response curve of response point 6 under different wind angles when the crowd density is 0.3 person/m².

From Fig. 15, when the wind angle is 0 degrees, the vertical peak acceleration of the structure increases continuously with crowd density. In contrast, the horizontal lateral peak acceleration of the structure decreases with the rise of crowd density. The horizontal lateral peak acceleration decreased by 5.81% and the vertical peak acceleration increased by 380.27% for the crowd density of 0.5 person/m^2 condition compared to the crowd density of 0.1 person/m^2 condition. Meanwhile, the trends of the horizontal lateral acceleration response curves of the structure under different crowd densities are basically consistent. This phenomenon indicates that the degree of influence of pedestrian load on the horizontal lateral vibration response of the structure is much smaller than its influence on the vertical vibration response of the structure.

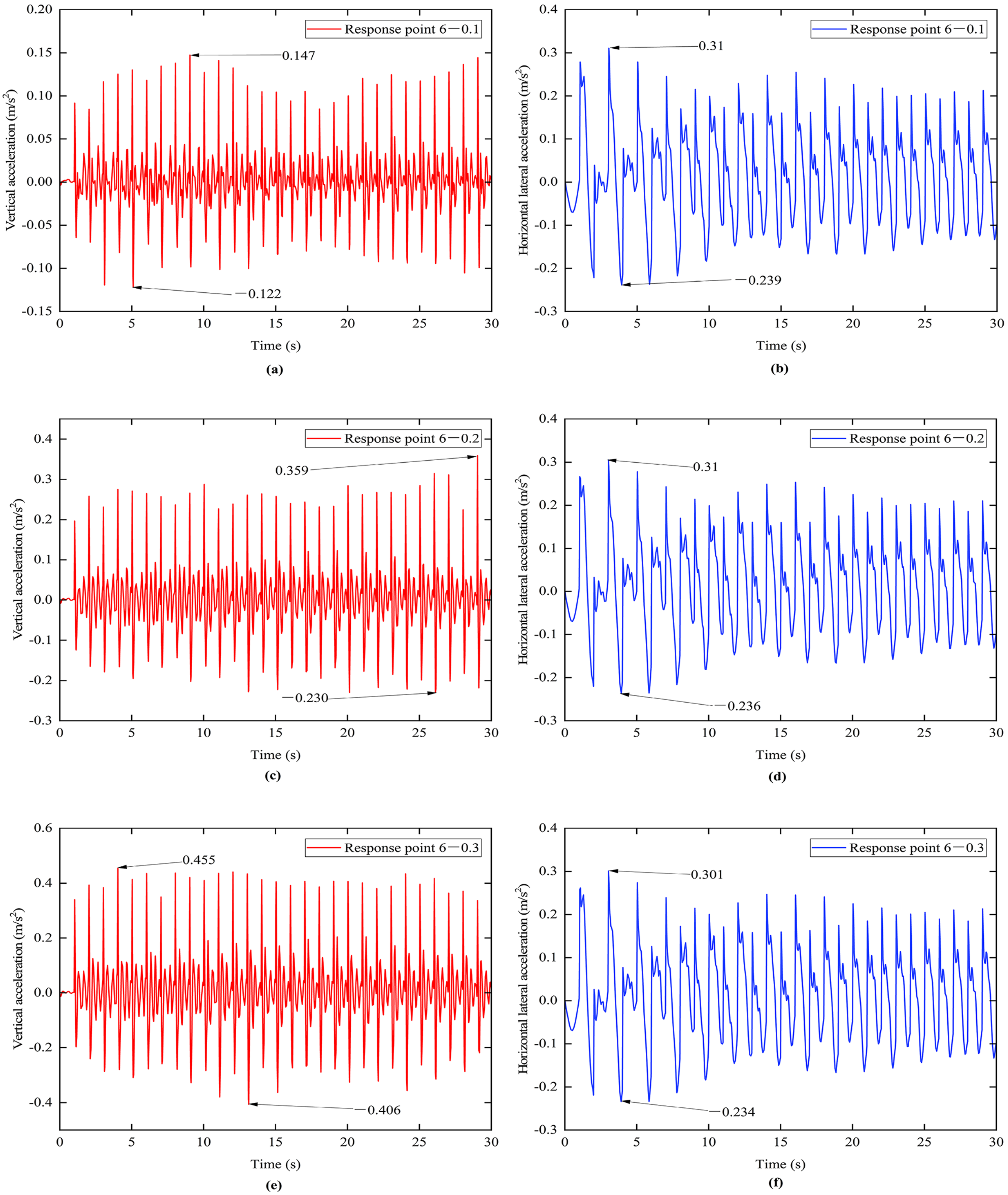

Fig. 15. The time-course curve of acceleration response under different pedestrian load coupling conditions at the 0-degree wind angle.

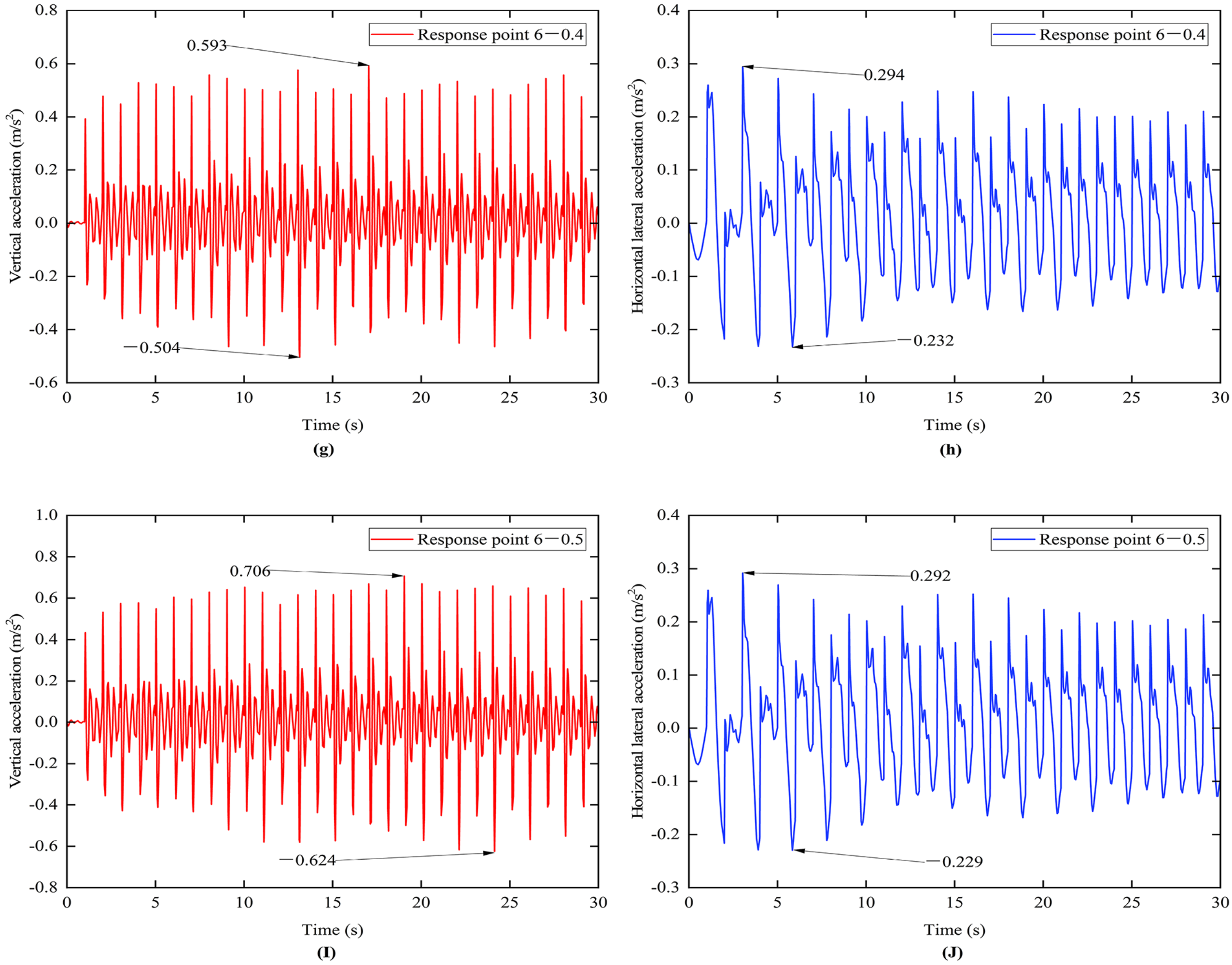

Figure 15. (continued)

From Fig. 16, at a crowd density of 0.3 persons/m^2, the vertical peak acceleration of the large-span double-connected structure basically remains stable with the increase of wind angle, fluctuating up and down from − 5.93 to 8.13%. The horizontal lateral peak acceleration of the structure decreases with the increase of wind angle. The horizontal lateral peak acceleration decreases by 39.2% in the case of a 45-degree wind angle compared to the case of a 0-degree wind angle and decreases by 83.39% in the case of a 90-degree wind angle compared to the case of a 0-degree wind angle. This phenomenon indicates that wind load is the main contributor to the horizontal lateral vibration response of the structure, while the effect of different wind angles on the horizontal lateral vibration response of the structure must be considered. In addition, wind loads have some degree of influence on the vertical vibration response of the structure.

To better assess the impact of various locations and load-coupling conditions on the dynamic response of the large-span double-connected structure. We analyzed the peak acceleration of the structure at different locations under the same load-coupled condition and the peak acceleration of the structure at the same location under different load-coupled conditions, as shown in Figs. 17 and 18, respectively. The time-course curve of acceleration response in the span of the spatial large-span corridor and at the connection with the main body on both sides is shown in Fig. 19 below.

From Fig. 17(a) and Fig. 18(a), the horizontal lateral peak acceleration of the large-span biconnected structure increases with increasing height. This is because the wind speed increases with the increase in the height of the large-span double-connected structure, which in turn leads to an increase in the horizontal lateral peak acceleration of the structure. However, the horizontal lateral peak acceleration of the structure shows a decrease with increasing wind angle. The horizontal lateral peak accelerations of the left and right sides of the main body of the large-span double-connected structure at the same height are basically the same when coupled with five pedestrian loading conditions at a 0-degree wind angle. However, at the same height, the horizontal lateral peak acceleration at the mid-span location of the connecting corridor is 10.57–13.14% higher than that at the mid-span location of the main body on the left and right sides. For the five pedestrian loading conditions coupled at a 45-degree wind angle, the structure has a larger horizontal lateral peak acceleration at the same height at the left main body mid-span location than at the connecting corridor mid-span location. The horizontal lateral peak

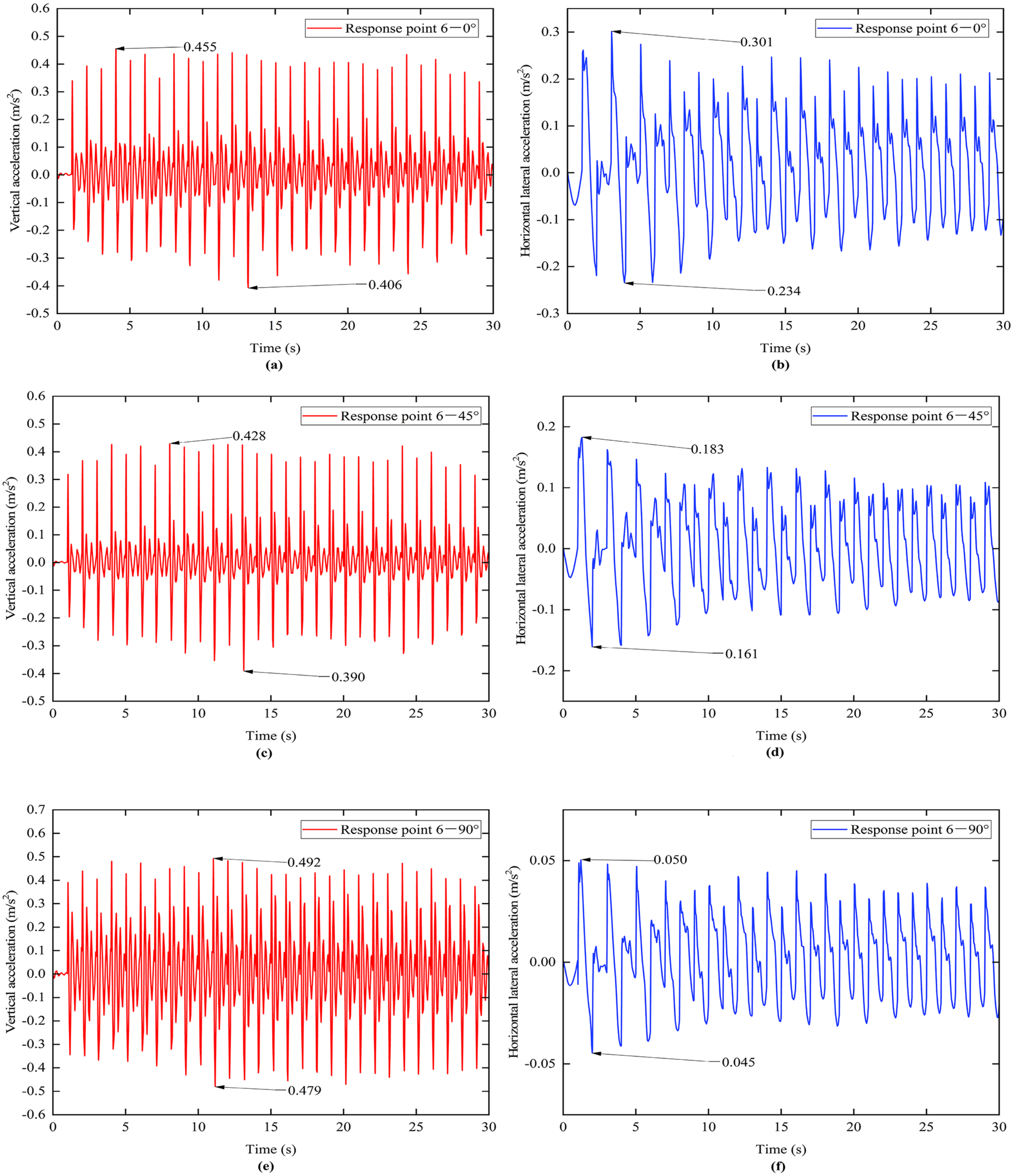

Fig. 16. The time-course curve of acceleration response under different wind angle coupling conditions when the crowd density is 0.3 person/m^2.

acceleration at the mid-span position of the connecting corridor is larger than that at the mid-span position of the right main body. The horizontal lateral peak acceleration of the large-span double-connected structure does not change significantly with height for the five pedestrian loading conditions coupled at 90-degree wind angles. This is because the effective area of the lateral windward surface of the structure in the plane where the XY axis is located decreases as the wind angle increases, which in turn leads to a decrease in the horizontal lateral peak acceleration of the structure.

Based on Fig. 17(b) and Fig. 18(b), the vertical vibration response of the large-span double-connected structure primarily occurs within the connecting corridor area under pedestrian loads. The response points

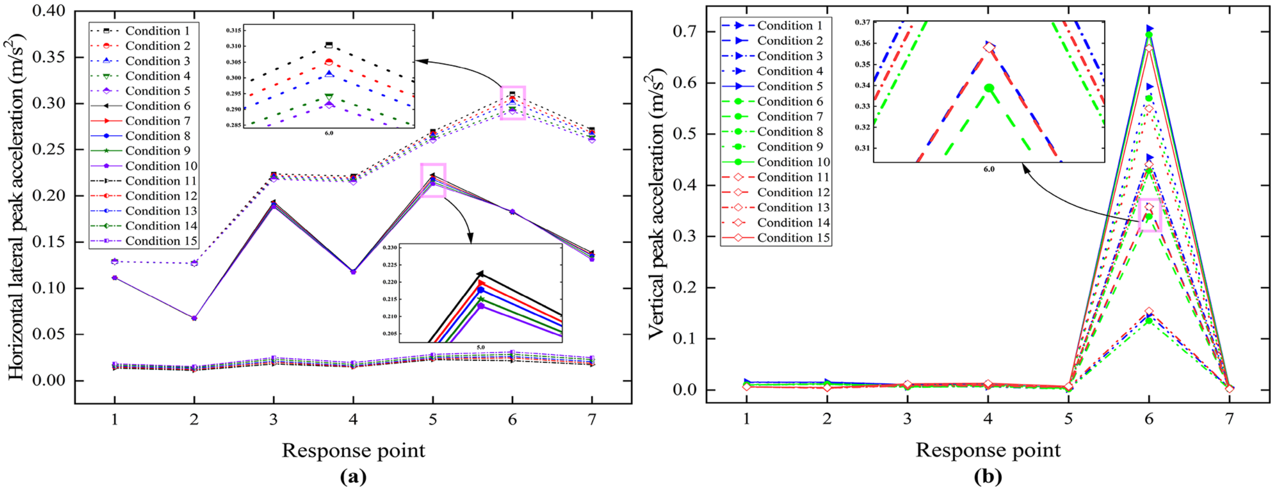

(a) (b)

Fig. 17. Peak acceleration response of the structure at different locations for the same load-coupled condition.

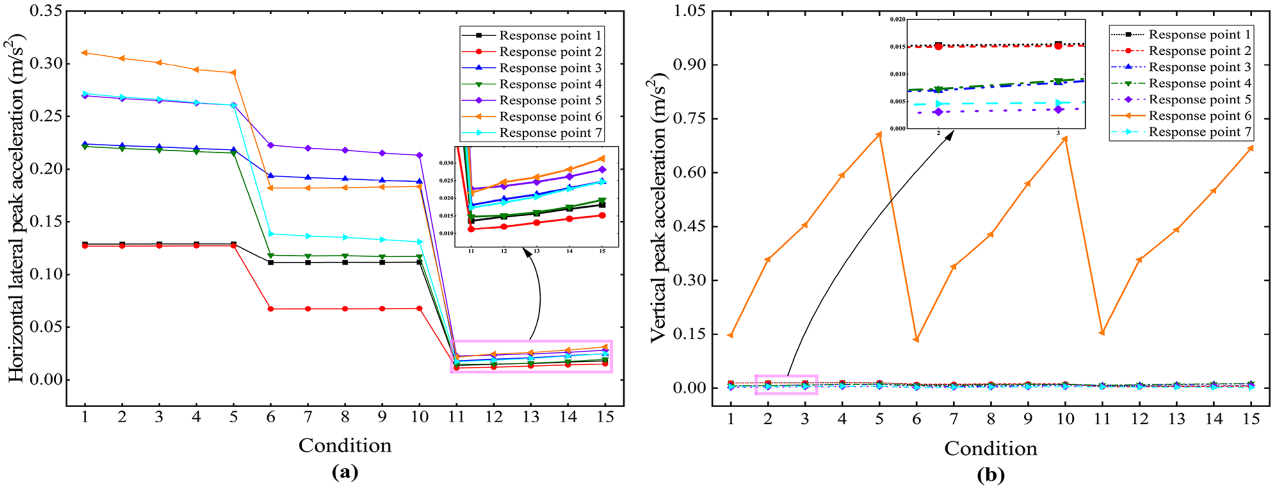

(a) (b)

Fig. 18. Peak acceleration response of the structure at the same location under different load coupling conditions.

located at the left and right main body sections of the structure show negligible influence from pedestrian loads. The vertical peak acceleration at the mid-span location of the connecting corridor shows an increase with the increase in crowd density.

Based on Fig. 19, the horizontal lateral acceleration response at the mid-span of the spatial large-span corridor and its connection position with the main body is generally consistent across different working conditions. However, the peak acceleration at the mid-span is slightly higher than at the connection position with the main body. In contrast, the vertical acceleration response at the mid-span is significantly more pronounced compared to the connection position with the main body. Consequently, only the mid-span position of the spatial large-span corridor will be considered in the subsequent comfort assessment.

Vibration suitability assessment of the large-span double-connected structure

The assessment of structural vibration suitability is usually measured by the natural frequency and peak acceleration of the structure[14]. Table 10 lists the corresponding limits proposed by some codes.

As shown in Tables 3 and 10, the horizontal lateral and vertical vibrations of the large-span double-connected structure are in the sensitive frequency range. In this study, the vibration suitability of the large-span double-connected structure is evaluated according to different codes. Given that the pedestrian loads are only applied to the connecting corridor, this study only evaluates the vertical comfort at the location of the connecting corridor. We have tabulated the peak accelerations of the large-span double-connected structure at different heights and under different load-coupling conditions, as shown in Table 11.

From Table 11, according to the EN03 code, the vertical comfort level of the spatial large-span corridor is mean or max under all load cases. Except for the spatial large-span corridor, the horizontal lateral comfort level

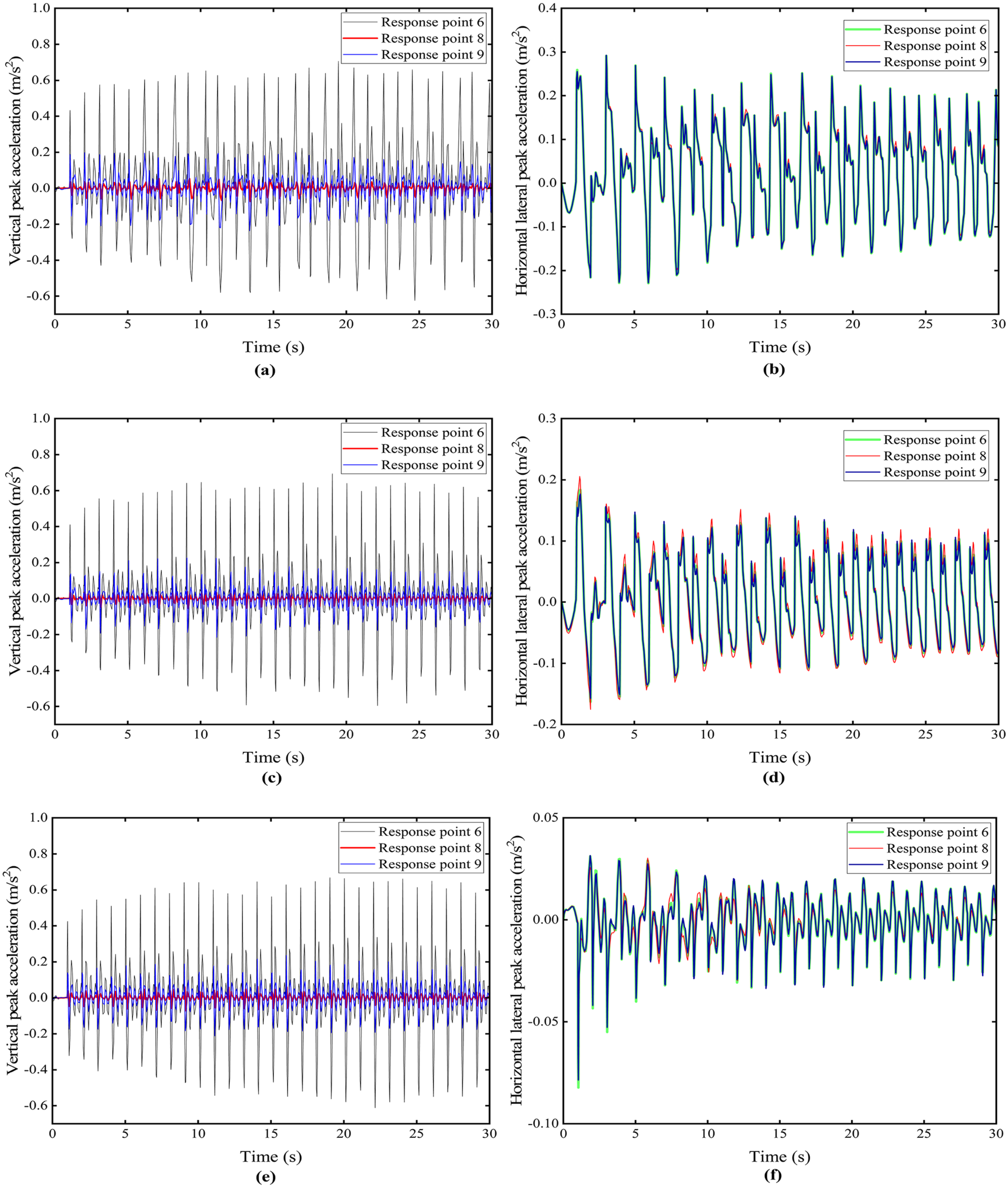

Fig. 19. The time-course curves of acceleration response at different locations of the spatial large-span corridor.

of the large-span double-connected structure is mean or max under all load conditions. Under the condition of a 0-degree wind angle, when the crowd density does not exceed 0.3 person/m^2, the horizontal lateral comfort level of the spatial large-span corridor is the min. when the crowd density exceeds 0.3 person/m^2, the horizontal lateral comfort level of the spatial large-span corridor is mean, which shows the phenomenon that the comfort level increases with the increase of crowd density to a certain extent. Under the rest of the load conditions, the horizontal lateral comfort level of the spatial large-span corridor reaches mean or max. According to the JGJ99-2015 code, the vertical peak acceleration of the spatial large-span corridor exceeds the comfort limit requirement

	Frequency limit		Acceleration limit		
Code	Vertical (Hz)	Horizontal (Hz)	Vertica (m/s^2)		Horizontal (m/s^2)
EN03[43]	1st order:1.25–2.3 2nd order: 2.5–4.6	0.5–1.2	Max: <0.5 Mean: 0.5–1.0 Min: 1.0–2.5 Unacceptable: > 2.5		Max: <0.1 Mean: 0.1–0.3 Min: 0.3–0.8 Unacceptable: > 0.8
Technical Standard for Human Comfort of the Floor Vibration [44]	>3	>1.2	Enclosed corridor: <0.15 Unenclosed corridor: <0.5		<0.1
Technical Specification for Steel Structure of Tall Building[45]	>3		Flat, office	0.07 (<2 Hz)	Office, hotel: <0.28
				0.05 (≥ 4 Hz)	
			Shopping center and indoor corridor	0.22 (<2 Hz)	Houses, flats: <0.2
				0.15 (≥ 4 Hz)	

Table 10. Design parameters and limitations for different codes.

of the code for the rest of the loading conditions, except for loading condition 1 and loading condition 6. When the purpose of the large-span double-connected structure is office or hotel, except for the spatial large-span corridor, its horizontal lateral peak acceleration meets the comfort limit requirements of the code. In the case of a 0-degree wind angle load, the horizontal lateral peak acceleration of the spatial large-span corridor does not meet the comfort limit requirements of the code. The horizontal lateral peak acceleration under the remaining load cases meets the comfort limits of the code. When the use of the large-span double-connected structure is houses or flats, the horizontal lateral comfort level of the structure is significantly affected by the position of the structure and the wind direction. Under the condition of 0-degree wind angle load, the horizontal lateral peak acceleration at all response points does not satisfy the code comfort limits, except for response points 1 and 2, where the horizontal lateral peak acceleration satisfies the code comfort limits. For the rest of the wind angle loading cases, the horizontal lateral peak acceleration of the response points satisfies the code comfort limits, except for response point 5 with a 45-degree wind angle, which does not satisfy the code comfort limits. This phenomenon is related to the location of the distribution of the effective windward area of the large-span double-connected structure at different wind angles.

Conclusion

Currently, extensive research has been conducted on the vibration response of structures under pedestrian loads or wind loads, but there remains a relative dearth of studies on their response to the combined effects of pedestrian and wind loads. In this paper, the structural vibration response of the large-span double-connected structure under combined pedestrian and wind loads is investigated by simulating random pedestrian and wind loads based on an actual project. The findings contribute valuable insights into the dynamic response and vibration suitability assessment of such structures under coupled pedestrian and wind loading conditions. The research demonstrates that:

1. For buildings with unique shapes, the wind load body shape coefficient on their surfaces can be determined through simulated wind tunnel tests.
2. For the large-span double-connected structure, the presence of rectangular apertures exacerbates the dynamic response of the structure. The dynamic response at the spatial large-span corridor is more intense than that of the main body on both sides, and the most unfavorable response point occurs at the mid-span position of the spatial large-span corridor. The most unfavorable wind angle of the structure is a 0-degree wind angle, and the vertical peak acceleration of the structure is 0.7063 m/s^2, which is reached at the crowd density of 0.5 persons/m^2. The horizontal lateral peak acceleration of the structure is 0.3104 m/s^2, which is reached at a crowd density of 0.1 persons/m^2.
3. For the dynamic response of a structure under coupled wind and pedestrian loads, the pedestrian loads control the vertical response of the structure, while the wind loads control the horizontal lateral response of the structure. However, the presence of wind loads will inhibit the vertical response of the structure caused by pedestrian loads and improve the vertical comfort of the structure to some extent. With the increase in crowd density, the peak vertical acceleration of the structure considering the coupled effect of wind and pedestrian loads is reduced by 2.56–9.84% compared to that when only pedestrian loads are considered. The effect of pedestrian loads on the horizontal lateral response of the structure is much smaller than that of wind loads.
4. The JGJ99-2015 code has more stringent requirements for structural comfort than the EN03 code. When assessing the vertical comfort of structures, it is more reasonable to use the EN03 code. When assessing the horizontal lateral comfort of structures, it is more reasonable to use the JGJ99-2015 code.
5. The optimum vertical comfort level for the spatial large-span corridor is achieved when the crowd density does not exceed 0.3 persons/m^2. As the crowd density continues to increase, the level of structural comfort

Response point	Load coupling condition	Vertical peak acceleration (m/s^2)	Comfort level		Horizontal lateral Peak acceleration (m/s^2)	Comfort level JGJ99-2015		
			EN03	JGJ99-2015		EN03	Office, hotel	Houses, flats
1	1	0.0150	\	\	0.1288	Mean	Acceptable level	Acceptable level
	2	0.0153			0.1288			
	3	0.0154			0.1289			
	4	0.0159			0.1289			
	5	0.0154			0.1290			
	6	0.0096			0.1114			
	7	0.0098			0.1114			
	8	0.0101			0.1114			
	9	0.0108			0.1114			
	10	0.0104			0.1117			
	11	0.0064			0.0136	Max		
	12	0.0063			0.0148			
	13	0.0061			0.0157			
	14	0.0058			0.0170			
	15	0.0063			0.0182			
2	1	0.0147	\	\	0.1269	Mean	Acceptable level	Acceptable level
	2	0.0150			0.1270			
	3	0.0151			0.1271			
	4	0.0156			0.1271			
	5	0.0155			0.1271			
	6	0.0111			0.0673	Max		
	7	0.0113			0.0674			
	8	0.0116			0.0674			
	9	0.0121			0.0675			
	10	0.0123			0.0677			
	11	0.0038			0.0112			
	12	0.0040			0.0119			
	13	0.0044			0.0131			
	14	0.0049			0.0142			
	15	0.0050			0.0151			
3	1	0.0064	\	\	0.2236	Mean	Acceptable level	Unacceptable level
	2	0.0070			0.2220			
	3	0.0084			0.2208			
	4	0.0100			0.2193			
	5	0.0108			0.2181			
	6	0.0056			0.1935			Acceptable level
	7	0.0055			0.1918			
	8	0.0062			0.1907			
	9	0.0072			0.1892			
	10	0.0089			0.1882			
	11	0.0081			0.0181	Max		
	12	0.0089			0.0197			
	13	0.0099			0.0211			
	14	0.0114			0.0230			
	15	0.0123			0.0247			

Continued

Response point	Load coupling condition	Vertical peak acceleration (m/s^2)	Comfort level		Horizontal lateral Peak acceleration (m/s^2)	Comfort level JGJ99-2015		
			EN03	JGJ99-2015		EN03	Office, hotel	Houses, flats
4	1	0.0067	\	\	0.2213	Mean	Acceptable level	Unacceptable level
	2	0.0073			0.2194			
	3	0.0088			0.2181			
	4	0.0103			0.2165			
	5	0.0114			0.2151			
	6	0.0077			0.1183			Acceptable level
	7	0.0072			0.1179			
	8	0.0088			0.1181			
	9	0.0101			0.1172			
	10	0.0107			0.1173			
	11	0.0081			0.0148	Max		
	12	0.0096			0.0151			
	13	0.0109			0.0160			
	14	0.0121			0.0176			
	15	0.0133			0.0195			
5	1	0.0021	\	\	0.2696	Mean	Acceptable level	Unacceptable level
	2	0.0031			0.2670			
	3	0.0035			0.2651			
	4	0.0042			0.2625			
	5	0.0047			0.2601			
	6	0.0017			0.2224			
	7	0.0026			0.2197			
	8	0.0032			0.2178			
	9	0.0037			0.2151			
	10	0.0041			0.2131			
	11	0.0051			0.0227	Max		Acceptable level
	12	0.0055			0.0235			
	13	0.0059			0.0247			
	14	0.0068			0.0262			
	15	0.0075			0.0281			
6	1	0.1474	Max	Acceptable level	0.3104	Min	Unacceptable level	Unacceptable level
	2	0.3588		Unacceptable level	0.3051			
	3	0.4546			0.3011			
	4	0.5930	Mean		0.2942	Mean		
	5	0.7063			0.2915			
	6	0.1351	Max	Acceptable level	0.1821		Acceptable level	Acceptable level
	7	0.3388		Unacceptable level	0.1821			
	8	0.4281			0.1825			
	9	0.5700	Mean		0.1831			
	10	0.6942			0.1835			
	11	0.1546	Max		0.0215	Max		
	12	0.3580			0.0246			
	13	0.4412			0.0260			
	14	0.5500	Mean		0.0282			
	15	0.6679			0.0312			
Continued								

Response point	Load coupling condition	Vertical peak acceleration (m/s^2)	Comfort level		Horizontal lateral Peak acceleration (m/s^2)	Comfort level JGJ99-2015		
			EN03	JGJ99-2015		EN03	Office, hotel	Houses, flats
7	1	0.0038	\	\	0.2716	Mean	Acceptable level	Unacceptable level
	2	0.0046			0.2683			
	3	0.0047			0.2662			
	4	0.0053			0.2631			
	5	0.0057			0.2605			
	6	0.0020			0.1384			Acceptable level
	7	0.0026			0.1363			
	8	0.0031			0.1352			
	9	0.0038			0.1330			
	10	0.0044			0.1310			
	11	0.0035			0.0174	Max		
	12	0.0032			0.0188			
	13	0.0026			0.0204			
	14	0.0022			0.0227			
	15	0.0020			0.0247			

Table 11. Dynamic response information of the large-span double-connected structure under different load coupling conditions.

decreases. The horizontal lateral comfort of the structure is strongly influenced by the height of the structure and the wind angle. As the wind angle increases, the effective area of the lateral windward surface of the structure in the plane of the XY axis decreases, which in turn affects the horizontal lateral acceleration of the structure.

Data availability

The datasets used in this study are available upon request from the corresponding author.

Received: 10 July 2024; Accepted: 16 September 2024

References

1. Kwok, K. C. S., Hitchcock, P. A. & Burton, M. D. Perception of vibration and occupant comfort in wind-excited tall buildings. *J. WIND Eng. Ind. Aerodyn.* **97**, 368–380. https://doi.org/10.1016/j.jweia.2009.05.006 (2009).
2. Schlaich, M. et al. *Fib Bulletin 32. Guidelines for the Design of Footbridges* (fib. The International Federation for Structural Concrete, 2005).
3. Dallard, P. The London Millennium Footbridge. 79, (2001).
4. Billah, K. Y., Scanlan, R. H. & Resonance Tacoma Narrows bridge failure, and undergraduate physics textbooks. *Am. J. Phys.***59**, 118–124. https://doi.org/10.1119/1.16590 (1991).
5. Piccardo, G. & Tubino, F. Equivalent spectral model and maximum dynamic response for the serviceability analysis of footbridges. *Eng. Struct.***40**, 445–456. https://doi.org/10.1016/j.engstruct.2012.03.005 (2012).
6. Lee, S. H., Lee, K. K., Woo, S. S. & Cho, S. H. Global vertical mode vibrations due to human group rhythmic movement in a 39 story building structure. *Eng. Struct.***57**, 296–305. https://doi.org/10.1016/j.engstruct.2013.09.035 (2013).
7. Chen, J., Xu, R. & Zhang, M. Acceleration response spectrum for predicting floor vibration due to occupant walking. *J. Sound Vib.***333**, 3564–3579. https://doi.org/10.1016/j.jsv.2014.03.023 (2014).
8. Chen, J., Li, G. & Racic, V. Acceleration response spectrum for predicting floor vibration due to occupants jumping. *Eng. Struct.***112**, 71–80. https://doi.org/10.1016/j.engstruct.2016.01.013 (2016).
9. Chen, J., Wang, L., Racic, V. & Lou, J. Acceleration response spectrum for prediction of structural vibration due to individual bouncing. *Mech. Syst. Signal. Process.***76–77**, 394–408. https://doi.org/10.1016/j.ymssp.2016.02.032 (2016).
10. Basaglia, B. M., Li, J., Shrestha, R. & Crews, K. Response prediction to walking-Induced vibrations of a long-span timber floor. *J. Struct. Eng.***147**, 04020326. https://doi.org/10.1061/(ASCE)ST.1943-541X.0002888 (2021).
11. Cao, L., Liu, J., Zhou, X. & Chen, Y. F. Vibration performance characteristics of a long-span and light-weight concrete floor under human-induced loads. *Struct. Eng. Mech.***65**, 349–357. https://doi.org/10.12989/sem.2018.65.3.349 (2018).
12. Chen, Z. et al. Dynamic Response Analysis and Vibration Reduction of Steel Truss Corridor Pedestrian Bridge under Pedestrian load. *Front. Mater.***9**, 839265. https://doi.org/10.3389/fmats.2022.839265 (2022).
13. Štěpánek, J. & Máca, J. RELATION BETWEEN STATIONARY AND MOVING PEDESTRIAN LOAD MODELS. *Acta Polytech. CTU Proc.***15**, 114–119. https://doi.org/10.14311/APP.2018.15.0114 (2018).
14. Dey, P., Narasimhan, S. & Walbridge, S. Reliability-based assessment and calibration of standards for the lateral vibration of pedestrian bridges. *Eng. Struct.***239**, 112271. https://doi.org/10.1016/j.engstruct.2021.112271 (2021).
15. Goto, T. Studies on wind-induced motion of tall buildings based on occupants' reactions. *J. Wind Eng. Ind. Aerodyn.* **13**, 241–252. https://doi.org/10.1016/0167-6105(83)90145-9 (1983).
16. Lamb, S., Kwok, K. C. S. & Walton, D. Occupant comfort in wind-excited tall buildings: motion sickness, compensatory behaviours and complaint. *J. Wind Eng. Ind. Aerodyn.* **119**, 1–12. https://doi.org/10.1016/j.jweia.2013.05.004 (2013).
17. Lamb, S., Kwok, K. C. S. & Walton, D. A longitudinal field study of the effects of wind-induced building motion on occupant wellbeing and work performance. *J. Wind Eng. Ind. Aerodyn.* **133**, 39–51. https://doi.org/10.1016/j.jweia.2014.07.008 (2014).
18. Lamb, S. & Kwok, K. C. S. The fundamental human response to wind-induced building motion. *J. WIND Eng. Ind. Aerodyn.* **165**, 79–85. https://doi.org/10.1016/j.jweia.2017.03.002 (2017).

19. Wang, Q. & Zhang, B. Wind-Induced responses and wind loads on a Super high-rise building with various cross-sections and high side Ratio—A case study. *Buildings*. **13**, 485. https://doi.org/10.3390/buildings13020485 (2023).
20. Li, Y., Yin, J. & Zhang, Y. Effects of Corner Set – backs on wind loads and wind Induced responses of rectangular tall buildings. *Appl. Sci.***12**, 12742. https://doi.org/10.3390/app122412742 (2022).
21. Wang, X. *Ansys Structural Dynamic Analysis with Applications*. (China Communications).
22. Aghabeigi, P. & Farahmand-Tabar, S. Seismic vulnerability assessment and retrofitting of historic masonry building of Malek Timche in Tabriz Grand Bazaar. *Eng. Struct.***240**, 112418. https://doi.org/10.1016/j.engstruct.2021.112418 (2021).
23. *GB50009-2012*. Building Structural Load Code. China Architecture & Building: Beijing, China, (2012).
24. Živanović, S., Pavić, A. & Reynolds, P. Probability-based prediction of multi-mode vibration response to walking excitation. *Eng. Struct.***29**, 942–954. https://doi.org/10.1016/j.engstruct.2006.07.004 (2007).
25. Li, J. & Chen, J. *Stochastic Dynamics of Structures* (John Wiley & Sons, Ltd, 2009). https://doi.org/10.1002/9780470824269
26. Zhao, D. S. & Chen, J. Tests for correlation and modeling of individual 3-D continuous walking load. *J. Vib. Shock*. **38**, 166–172. https://doi.org/10.13465/j.cnki.jvs.2019.11.025 (2019).
27. Chen, J., Wang, H. Q. & Peng, Y. X. Experimental investigation on Fourier-series model of walking load and its coefficients. *J. Vib. Shock*. **33**, 11–15. https://doi.org/10.13465/j.cnki.jvs.2014.08.003 (2014). +28.
28. Chen, J., Peng, Y. X. & Wang, L. Experimental investigation and mathematical modeling of single footfall load using motion capture technology. *China Civ. Eng. J.***47**, 79–87. https://doi.org/10.15951/j.tmgcxb.2014.03.012 (2014). https://link.cnki.net/doi/
29. Wang, J. & Chen, J. A comparative study on different walking load models. *Struct. Eng. Mech.***63**, 847–856. https://doi.org/10.12989/sem.2017.63.6.847 (2017).
30. Yang, S. W. et al. Dynamic response study of Space large-span structure under Stochastic Crowd-Loading Excitation. *Buildings*. **14**, 1203. https://doi.org/10.3390/buildings14051203 (2024).
31. Li, C., Pan, H., Tian, L. & Bi, W. Lifetime multi-hazard fragility analysis of transmission towers under earthquake and wind considering wind-induced fatigue effect. *Struct. Saf.***99**, 102266. https://doi.org/10.1016/j.strusafe.2022.102266 (2022).
32. Kaimal, J. C., Wyngaard, J. C., Izumi, Y. & Coté, O. R. Spectral characteristics of surface-layer turbulence. *Q. J. R Meteorol. Soc.***98**, 563–589. https://doi.org/10.1002/qj.49709841707 (1972).
33. Wang, D., Zhou, Y. & Zhu, Y. Vibration control study on a supertall building. *Struct. Des. Tall Spec. Build.***21**, 28–45. https://doi.org/10.1002/tal.618 (2012).
34. Liu, J., Li, Z., Liu, W., Hu, C. & Zhang, C. Design and characteristics analysis of a new vibration reduction system for in service long span transmission tower. *Sci. Rep.***12**, 11373. https://doi.org/10.1038/s41598-022-15659-9 (2022).
35. Wang, X. Q. & Cui, J. F. Formula of Coefficient K in expression of Davenport Spectrum and its Engineering Application. *J. Tongji Univ. (Natural Science)* 849–852 (2002).
36. A.g, D. The dependence of wind loads on meteorological parameters. (1967).
37. Tamura, Y., Kawai, H., Uematsu, Y., Okada, H. & Ohkuma, T. Documents for wind resistant design of buildings in Japan.
38. Zhang, L., Jia, J. & Dong, L. Study on wind load characteristics and wind-Induced response of Supertall buildings with single-sided large-span straight platforms. *Buildings*. **12**, 1694. https://doi.org/10.3390/buildings12101694 (2022).
39. JGJ/T338. - The standard for Wind Tunnel Test Methods for Construction Projects. China Architecture & Building Press: Beijing, China, 2014. (2014).
40. Xie, S. et al. Numerical Simulation and Wind Tunnel Test on the Wind-Induced Response of Three Typical Types of Greenhouse Main Structures. *Agriculture* 12, 1294 (2022). https://doi.org/10.3390/agriculture12091294
41. Kim, R., Lee, I. & Kwon, K. Evaluation of wind pressure acting on multi-span greenhouses using CFD technique, part 1: development of the CFD model. *Biosyst Eng.***164**, 235–256. https://doi.org/10.1016/j.biosystemseng.2017.09.008 (2017).
42. Jones, W. P. & Launder, B. E. The prediction of laminarization with a two-equation model of turbulence. *Int. J. Heat. Mass. Transf.***15**, 301–314. https://doi.org/10.1016/0017-9310(72)90076-2 (1972).
43. HiVoSS. *Human Induced Vibrations of Steel Structures: Design of Footbridges* (European Communities: Luxembourg,, 2008).
44. JGJ/T441-. Technical Standard for Human Comfort of the Floor Vibration. China Architecture & Building Press: Beijing, China, 2019. (2019).
45. JGJ99-. Technical Specification for Steel Structure of Tall Building. China Architecture & Building Press: Beijing, China, 2016. (2015).

Author contributions

The contributions made by the authors are described as follows: S.Y.: Conceptualization, Methodology, Writing-Original draft preparation. Q.X.: Investigation, Writing-Reviewing and Editing. G.W.: Software, Data curation. J.H.: Supervision, Investigation, Methodology. M.Y.: Conceptualization, Writing-Reviewing and Editing. Z.Z.: Writing-Reviewing and Editing, Data curation. All authors reviewed the manuscript.

Declarations

Competing interests

The authors declare no competing interests.

Additional information

Correspondence and requests for materials should be addressed to Q.X.

Additional information

Correspondence and requests for materials should be addressed to Q.X.

Reprints and permissions information is available at www.nature.com/reprints.